

## Cosmic distributions of stellar tidal disruptions by massive black holes at galactic centers

YUNFENG CHEN,<sup>1</sup> QINGJUAN YU,<sup>1</sup> AND YOUJUN LU<sup>2,3</sup><sup>1</sup>*Kavli Institute for Astronomy and Astrophysics, and School of Physics, Peking University, Beijing, 100871, China*<sup>2</sup>*National Astronomical Observatories, Chinese Academy of Sciences, Beijing, 100012, China*<sup>3</sup>*School of Astronomy and Space Science, University of Chinese Academy of Sciences, Beijing 100049, China*

## ABSTRACT

Stars can be consumed (either tidally disrupted or swallowed whole) by massive black holes (MBHs) at galactic centers when they move into the vicinity of the MBHs. In this study, we investigate the rates of stellar consumptions by central MBHs and their cosmic distributions, including the effects of triaxial galaxy shapes in enhancing the reservoir of low-angular-momentum stars and incorporating realistic galaxy distributions. We find that the enhancement in the stellar consumption rates due to triaxial galaxy shapes can be significant, by a factor of  $\sim 3$  for MBH mass  $M_{\text{BH}} \sim 10^5\text{--}10^6 M_{\odot}$  and up to more than one order of magnitude for  $M_{\text{BH}} \gtrsim 10^8 M_{\odot}$ . Only for  $M_{\text{BH}} \lesssim 10^7 M_{\odot}$  are the stellar consumption rates significantly higher in galaxies with steeper inner surface brightness profiles. The average (per galaxy) stellar consumption rates correlate with central MBH masses positively for  $M_{\text{BH}} \gtrsim 10^7 M_{\odot}$  and negatively for  $M_{\text{BH}} \lesssim 10^7 M_{\odot}$ . The volumetric stellar tidal disruption rates are  $\sim 3 \times 10^{-5} \text{yr}^{-1} \text{Mpc}^{-3}$  for MBHs in the mass range of  $10^5\text{--}10^8 M_{\odot}$  at  $z = 0$ ; and the volumetric stellar consumption rates by MBHs with higher masses are  $\sim 10^{-6} \text{yr}^{-1} \text{Mpc}^{-3}$ , which can be the stellar tidal disruption rate if the high-mass BHs are extremely spinning Kerr BHs or the rate of being swallowed if those BHs are Schwarzschild ones. The volumetric stellar consumption rates decrease with increasing redshift, and the decrease is relatively mild for  $M_{\text{BH}} \sim 10^5\text{--}10^7 M_{\odot}$  and stronger for higher  $M_{\text{BH}}$ . Most of the stellar tidal disruption events (TDEs) at  $z = 0$  occur in galaxies with mass  $M_{\text{gal}} \lesssim 10^{11} M_{\odot}$ , and about 1%–2% of the TDEs can occur in high-mass galaxies with  $M_{\text{gal}} \gtrsim 10^{11} M_{\odot}$ .

*Keywords:* Astrodynamics (76); Galaxy dynamics (591); Gravitational wave astronomy (675); High energy astrophysics (739); Supermassive black holes (1663); Tidal disruption (1696); Transient sources (1851); Time domain astronomy (2109).

## 1. INTRODUCTION

Stars can be tidally disrupted (or swallowed whole) by the massive black hole (MBH) at galactic centers when they move to the vicinity of the MBH (Hills 1975). Studies of stellar tidal disruption events (TDEs) produced by close encounters with MBHs are of interest in many aspects. The rich phenomena of TDEs provide not only a probe of much interesting physics in the vicinity of an

MBH (such as the relativistic effects, accretion physics, the interior structure of the torn stars, and the formation of radio jets via some jetted TDEs; e.g., Komossa 2015; Alexander 2017), but also a constraint on MBH properties and demographics (such as MBH spins, MBH occupation fractions in galaxies; e.g., Kesden 2012; Falikov & Loeb 2017). Stellar tidal disruptions are one possible channel that could contribute significantly to the present BH mass in faint galaxies (e.g.,  $\lesssim 10^9 L_{\odot}$ ) or low-mass MBHs (Magorrian & Tremaine 1999, hereafter MT99; Freitag & Benz 2002; Yu 2003; Brockamp et al. 2011; Alexander 2017). In addition, TDEs are among the astrophysical sources of gravitational wave radiation (e.g., Freitag 2003), and synergetic observa-

tions of the sources in both electromagnetic emission and gravitational wave radiation would shed new light on gravitational wave astrophysics. In this work, we investigate the expected TDE rates and their statistical distributions in the real universe.

The rates of TDEs have been estimated both observationally and theoretically. To date, a few dozen TDE candidates have been observed in the X-ray,  $\gamma$ -ray, UV, optical, infrared, and radio bands, and through emission lines, with  $\sim 1$ –3 new TDE candidates discovered every year (e.g., Komossa 2015; Alexander 2017; Stone et al. 2020). Based on these observational measurements, the TDE rate is estimated to be  $\sim 10^{-5}$ – $10^{-4}$ yr $^{-1}$ gal $^{-1}$  (e.g., Donley et al. 2002; Esquej et al. 2008; Maksym et al. 2010; Wang et al. 2012; van Velzen & Farrar 2014; Khabibullin & Sazonov 2014; Auchettl et al. 2018; van Velzen 2018), with large statistical uncertainty. With upcoming time-domain sky surveys, the size of the TDE sample is expected to expand by orders of magnitude (Komossa 2015; Stone et al. 2020), and thus the rates of TDEs in different types of galaxies can be determined with an improved statistics. The TDE rates have also been estimated analytically or numerically in many studies (e.g., MT99; Wang & Merritt 2004; Stone & Metzger 2016); and the estimates are typically about a few times  $10^{-4}$ yr $^{-1}$ gal $^{-1}$ , with the highest disruption rates occurring in faint cuspy galaxies. It is pointed out by Stone & Metzger (2016) that the analytical estimates appear to predict relatively more events, compared with those measured by observations.

The TDE rate in a galaxy depends on how frequently a star can move to a distance sufficiently close to the MBH to be tidally disrupted. Such a star has a low orbital angular momentum. After the initial low-angular-momentum stars in a stellar system are tidally disrupted (or swallowed whole) by the central MBH within one orbital period, the TDE rate depends on how frequently high-angular-momentum stars can refill low-angular-momentum orbits to have close interactions with the MBH. Most of the theoretical estimates of the TDE rates are mainly based on the refilling of stars onto the low-angular-momentum orbits by two-body relaxation. Some other mechanisms and phenomena have also been discussed to contribute to the TDEs or enhance the TDE rates, such as resonant relaxation (which is shown to enhance the overall rates only modestly; Rauch & Tremaine 1996; Hopman & Alexander 2006), the existence of massive perturbers at galactic centers (which is shown to increase the rate only by a factor of a few; Perets et al. 2007), the existence of a secondary MBH

at galactic centers (which is proposed to enhance the rate in a rather short dynamical friction timescale of  $\sim 10^5$  yr Ivanov et al. 2005; Chen et al. 2011), recoiled massive binary BH merger remnants (Stone & Loeb 2011), and non-spherical galaxy shapes (in which high-angular-momentum stars can precess onto low-angular-momentum orbits) (MT99; Yu 2002; Vasiliev & Merritt 2013; Vasiliev 2014). In this work, we consider the effects of triaxial galaxy shapes in enhancing the TDE rates.

The effects of non-spherical gravitational potentials on the TDE rates have been studied in some previous works (e.g., see MT99; Vasiliev & Merritt 2013), where either an axisymmetric galaxy shape configuration is generally assumed or a triaxial galaxy shape is assumed to evolve into an axisymmetric shape within a certain time period (e.g., one hundred times the orbital period) due to the existence of a central MBH in the stellar system (Merritt & Quinlan 1998). In this work, we assume that the triaxial shape of a galaxy is static, and we do not assume an evolution of triaxial shapes into axisymmetric shapes, which is plausible, at least, for the following reasons. (a) A small deviation from a purely axisymmetric configuration toward a triaxial one may lead to a much larger reservoir of stars that can move to the vicinity of the central MBHs (cf. Fig. 7 in Chen et al. 2020; hereafter CYL20). (b) The observations of the nuclear star cluster at our own Galactic center indicate that its shape can be triaxial even within the radius of the spherical influence of the central MBH (Feldmeier-Krause et al. 2017).

Note that the underlying physics in determining the TDE rates of stars by the central MBH in a triaxial galaxy has a similarity to that in determining the dynamical evolution timescale of a massive (hard) binary black holes (BBH) embedded in a triaxial galaxy merger remnant (Yu 2002). The former involves close interactions of stars with a single MBH, whereas the latter involves close interactions of stars with a hard BBH system. Both depend on how frequently low-angular-momentum stars can move to the vicinity of the MBHs. In CYL20, a statistical study has been done in how frequently stars can move to the BBH vicinity in realistic triaxial galaxy distributions, and further to obtain the distributions of the BBH evolution timescales, and the cosmic massive BBH populations, and their gravitational wave radiation. Due to the analogy, in this work it is straightforward to adopt many similar approaches and galaxy samples developed in CYL20 to obtain how frequently stars can move to the vicinity of

an MBH to be consumed with considering realistic triaxial galaxy distributions. For conciseness, in this paper we refer many relevant aspects (e.g., galaxy triaxiality shape distributions, galaxy surface brightness distributions, galaxy stellar mass functions, MBH demographics, the regions of the phase space in which stars that can precess onto low-angular-momentum orbits) directly to the relevant sections in CYL20.

This paper is organized as follows. In Section 2, we briefly describe the dynamical processes considered in this study that contribute to TDEs, and review the models for the rate of stellar consumption by the MBH in a galaxy, with including both the contributions by two-body relaxation and orbital precession in non-spherical galactic gravitational potentials. In Section 3, we present the framework for estimating the statistical distributions of the stellar consumption rates in galaxies with realistic distributions, as well as the galaxy samples, their distributions, and the BH demography to be used in the framework. The main results are presented in Section 4. Conclusions are given in Section 5.

## 2. LOSS-CONE REFILLING

Consider a stellar system consisting of a central MBH with mass  $M_{\text{BH}}$  and some surrounding stars. A star with mass  $m_*$  and radius  $r_*$  that can travel within a distance of  $r < r_t \simeq (f_t M_{\text{BH}}/m_*)^{1/3} r_*$  to the MBH will be disrupted by the tidal force from the central MBH if  $r_t > r_{\text{swl}}$ , or swallowed whole by the MBH if  $r_t < r_{\text{swl}}$ , where  $f_t$  is a factor related to the stellar structure and set to unity in this study,  $r_{\text{swl}} \equiv 4GM_{\text{BH}}/c^2$  (with including the general relativistic effect around a Schwarzschild BH; Chandrasekhar 1992),  $G$  is the gravitational constant, and  $c$  is the speed of light. The value of  $r_{\text{swl}}$  can be smaller/larger for a prograde/retrograde orbit if the MBH is a spinning Kerr BH. The disruption events are accompanied by luminous electromagnetic flares when the baryonic matter is stripped off the intruding star and accreted onto the MBH (Hills 1975; Rees 1988). Following MT99, we define the stellar “consumption rate” as the rate of stars moving to  $r < \max(r_t, r_{\text{swl}})$  and define the stellar “flaring rate” as the rate of stars moving to  $r < r_t$  with  $r_t > r_{\text{swl}}$ .

Given  $(\mathcal{E}, J)$ , where  $\mathcal{E}$  is the specific binding energy (hereafter energy) and  $J$  is the specific angular momentum (hereafter angular momentum) of a star, the loss

cone is defined as the phase space satisfying

$$J \leq J_{\text{lc}} \equiv \max(\sqrt{2r_t^2[\psi(r_t) - \mathcal{E}]}, J_{\text{swl}}) \quad (1)$$

$$\simeq \max(\sqrt{2GM_{\text{BH}}r_t}, J_{\text{swl}}),$$

where  $\psi(r) = -\Phi(r)$ ,  $\Phi(r)$  is the gravitational potential at distance  $r$  from the center,  $J_{\text{swl}} \equiv 4GM_{\text{BH}}/c$  for a Schwarzschild BH (with including the general relativistic effect; Chandrasekhar 1992). The loss cone in the context of BBH evolution can be set by replacing  $r_t$  by  $f_a a$ , where  $a$  is the separation of the binary system and  $f_a$  is a dimensionless factor  $\sim 1$  (Yu 2002).

The stars initially in the loss cone will be removed from the loss cone and consumed by the MBH within one orbital period. The long-term rate of stellar consumption by a central MBH is determined by the loss-cone refilling rate, i.e., how frequently the loss cone is refilled by stars initially outside the loss cone. In this work, we consider the refilling caused by both two-body relaxation and orbital precession in non-spherical gravitational potentials.

In non-spherical gravitational potentials, the phase space of  $(\mathcal{E}, J)$  in which the stars that can precess into the loss cone is described by “loss region”. The loss region can be approximated by a “loss wedge” [ $J_z < J_{\text{lc}}$  with  $J < J_s(\mathcal{E})$ , where  $J_z$  is the component of the  $J$  along the axisymmetric axis] for an axisymmetric system, and approximated by  $J < J_s(\mathcal{E})$  for a triaxial system. The  $J_s(\mathcal{E})$  is the characteristic angular momentum at energy  $\mathcal{E}$  below which the majority of stellar orbits are centrophilic. Both the loss wedge in an axisymmetric system and the loss region in a general triaxial system can be obtained by simulating stellar motion numerically (CYL20; Cui & Yu 2014) or by constructing a symplectic map in surfaces of section (Touma & Tremaine 1997; MT99). The rates of refilling into the loss cone caused by orbital precession constitute the long-term draining rates of the loss region. We adopt the relevant analytical results presented in MT99 on the stellar refilling rates caused by two-body relaxation and the draining rates of a full loss region, which are summarized in Sections 2.1 and 2.2, respectively.

Note that not only is the loss cone in a spherical stellar system refilled by two-body relaxation, but also the loss wedge/loss region in a non-spherical stellar system can be refilled by two-body relaxation. MT99 presents the analysis on the stellar diffusion into the loss wedge by two-body relaxation in an axisymmetric system. In this work, by generalizing the analytical result of stellar

diffusion into the loss cone in a spherical stellar system, we include the effect of stellar diffusion into the loss region by two-body relaxation in a triaxial system, and the corresponding analysis is presented in Section 2.1.

For simplicity, in this study we assume that the MBH at a galactic center is a single MBH. We ignore the effect of galaxy mergers, starbursts, mass growth, and the Brownian motion of the central MBH during the long-term period of stellar consumptions.

### 2.1. Two-body relaxation

The long-term diffusion rate of stars into the loss cone by two-body relaxation can be obtained by the steady-state solution of the Fokker-Planck equation. For simplicity, we assume that all the stars in the stellar system have the same mass  $m_*$  and radius  $r_*$ . As for a spectrum of stellar masses and radii, the derived diffusion rate differs by a factor  $\lesssim 2$  (e.g., Appendix A1 of MT99 and Section 2.3 of Stone & Metzger 2016).

We define  $R \equiv J^2/J_c^2(\mathcal{E})$  to be the dimensionless squared angular momentum, where  $J_c(\mathcal{E})$  is the angular momentum of a star at energy  $\mathcal{E}$  and on a circular orbit and we have  $R \leq 1$ . In a spherical system, the steady-state diffusion rate of stars into the loss cone obtained by solving the Fokker-Planck equation is given by (MT99; Lightman & Shapiro 1977; Cohn & Kulsrud 1978):

$$F^{\text{lc}}(\mathcal{E})d\mathcal{E} = \frac{F^{\text{max}}(\mathcal{E})d\mathcal{E}}{\ln R_0^{-1}(\mathcal{E})} = \frac{4\pi^2 P(\mathcal{E})J_c^2(\mathcal{E})\bar{\mu}(\mathcal{E})\bar{f}(\mathcal{E})d\mathcal{E}}{\ln R_0^{-1}(\mathcal{E})}, \quad (2)$$

where  $\bar{\mu}(\mathcal{E})$  is the orbit-averaged diffusion coefficient,  $\bar{f}(\mathcal{E})$  is the ‘isotropized’ distribution function (see Eq. 21 of MT99),  $F^{\text{max}}(\mathcal{E}) \equiv 4\pi^2 \bar{f}(\mathcal{E})J_c^2(\mathcal{E})\bar{\mu}(\mathcal{E})P(\mathcal{E})$  represents an estimate of the maximum possible flux through a surface of constant  $\mathcal{E}$  in phase space. The  $R_0$  in Equation (2) is given by

$$R_0(\mathcal{E}) = R_{\text{lc}}(\mathcal{E}) \times \begin{cases} \exp(-q) & q > 1 \\ \exp(-0.186q - 0.824\sqrt{q}) & q < 1 \end{cases} \quad (3)$$

where  $R_{\text{lc}}(\mathcal{E}) = J_{\text{lc}}^2(\mathcal{E})/J_c^2(\mathcal{E})$  and  $q(\mathcal{E}) \equiv P(\mathcal{E})\bar{\mu}(\mathcal{E})/R_{\text{lc}}(\mathcal{E})$  (MT99). The orbit-averaged diffusion coefficient,  $\bar{\mu}(\mathcal{E})$ , is defined by

$$\bar{\mu}(\mathcal{E}) \equiv \frac{2}{P(\mathcal{E})} \int_{r_-}^{r_+} \frac{\mu dr}{v_r} = \frac{-2}{P(\mathcal{E})} \int_0^\infty dv_r \frac{dr}{d\psi} \mu(\mathcal{E}, r), \quad (4)$$

where  $v_r$  is the radial velocity satisfying  $v_r = \sqrt{2(\psi(r) - \mathcal{E})}$ ,  $P(\mathcal{E})$  is the radial period of an orbit with

energy  $\mathcal{E}$  and zero angular momentum, and  $r_+$  and  $r_-$  are the apocenter and pericenter distances of loss-cone orbits. The diffusion coefficient  $\mu$  is defined as

$$\mu(\mathcal{E}, r) \equiv \langle (\Delta R)^2 \rangle / 2R \Big|_{R \rightarrow 0} = \frac{2r^2 \langle (\Delta v_t)^2 \rangle}{J_c^2(\mathcal{E})}, \quad (5)$$

where  $\langle (\Delta v_t)^2 \rangle$  is the diffusion coefficient for tangential velocity (Binney & Tremaine 2008), i.e.,

$$\langle (\Delta v_t)^2 \rangle = \frac{32\pi^2 G^2 m_*^2 \ln \Lambda}{3} \left( 3I_{\frac{1}{2}} - I_{\frac{3}{2}} + 2I_0 \right), \quad (6)$$

with

$$I_0 \equiv \int_0^\mathcal{E} \bar{f}(\mathcal{E}') d\mathcal{E}'$$

$$I_{\frac{n}{2}} \equiv [2(\psi(r) - \mathcal{E})]^{-\frac{n}{2}} \int_\mathcal{E}^{\psi(r)} [2(\psi(r) - \mathcal{E}')]^{\frac{n}{2}} \bar{f}(\mathcal{E}') d\mathcal{E}' \quad (7)$$

In an axisymmetric system, the diffusion rate of stars into the loss wedge by two-body relaxation, denoted by  $F^{\text{lw}}(\mathcal{E})$ , follows Equations (49) and (50) in MT99, where  $F^{\text{lw}}(\mathcal{E}) \leq F_{\text{full}}^{\text{lc}}(\mathcal{E})$  and  $F_{\text{full}}^{\text{lc}}(\mathcal{E}) \equiv 4\pi^2 f(\mathcal{E})J_{\text{lc}}^2(\mathcal{E})$  is the flux of stars per unit energy consumed by an MBH when the loss cone is full.

In a triaxial system, the diffusion rate of stars into the loss region by two-body relaxation, denoted by  $F^{\text{lr}}(\mathcal{E})$ , can be obtained by generalizing the analysis done for a spherical system, i.e., replacing  $J_c(\mathcal{E})$  by  $J_s(\mathcal{E})$  in Equations (2) and (3). In a triaxial system, the diffusion rate of stars into the loss region by two-body relaxation can contribute to the refilling rate of stars into the loss cone by  $F_{\text{tri}}^{\text{lc}}(\mathcal{E}) \equiv \min(F^{\text{lr}}(\mathcal{E}), F_{\text{full}}^{\text{lc}}(\mathcal{E}))$ . The difference of  $F_{\text{tri}}^{\text{lc}}(\mathcal{E})$  from  $F^{\text{lc}}(\mathcal{E})$  is one effect caused by the draining and depletion of the loss region in a triaxial system as described in Section 2.2.

### 2.2. Draining a full loss region in non-spherical gravitational potentials

In an axisymmetric or a triaxial system, initially the total stellar mass in the loss region is

$$M_{\text{lr}} \simeq m_* \int 4\pi^2 f(\mathcal{E})J_{\text{lr}}^2(\mathcal{E})P(\mathcal{E})d\mathcal{E}, \quad (8)$$

where  $J_{\text{lr}}^2 \equiv J_{\text{lc}}J_s(\mathcal{E})$  for an axisymmetric system and  $J_{\text{lr}}^2 \equiv J_s^2(\mathcal{E})$  for a triaxial system. At a sufficiently long time  $T$ , the draining rate of the loss region due to orbital

precession can be approximated by

$$F^{\text{drain}}(\mathcal{E})d\mathcal{E} = 4\pi^2 f(\mathcal{E})J_{\text{lc}}^2(\mathcal{E}) \exp\left[-\frac{T}{P(\mathcal{E})} \frac{J_{\text{lc}}^2(\mathcal{E})}{J_{\text{r}}^2(\mathcal{E})}\right] d\mathcal{E} \quad (9)$$

(cf. Eqs. 36 and 52 in MT99). In this work, the values of  $F^{\text{drain}}(\mathcal{E})$  used are set at a time  $T$  that is the Hubble time of the corresponding redshift. According to Equations (2) and (9), the ratio of the stellar consumption rate caused by orbital precession in the non-spherical potentials to that caused by two-body relaxation is given by

$$\frac{F^{\text{drain}}(\mathcal{E})}{F^{\text{lc}}(\mathcal{E})} = \frac{\ln R_0^{-1}(\mathcal{E})}{q(\mathcal{E})} \exp\left[-\frac{T}{P(\mathcal{E})} \frac{J_{\text{lc}}^2(\mathcal{E})}{J_{\text{r}}^2(\mathcal{E})}\right], \quad (10)$$

where  $\ln R_0^{-1}(\mathcal{E})/q(\mathcal{E}) \sim 1$  for  $q(\mathcal{E}) \gg 1$  and  $\ln R_0^{-1}(\mathcal{E})/q(\mathcal{E}) \sim -\ln R_{\text{lc}}/q(\mathcal{E})$  for  $q(\mathcal{E}) \rightarrow 0$ .

As presented above, the role of triaxiality of a galaxy is displayed through a characteristic angular momentum  $J_s(\mathcal{E})$ , which determines the size of the loss region. In this work, given the mass density distribution and the triaxial shape of a host stellar system, we use the Monte Carlo method to obtain  $J_s(\mathcal{E})$  by numerically simulating the motion of stars under the combined gravitational potential of a central point mass MBH and the galactic stars (with a triaxial gravitational potential shape) and finding out the fractions of stars on centrophilic orbits. The detailed numerical methods can be seen in Section 2.5 in CYL20. Note that a galaxy shape is likely to be close to being axisymmetric. In practice, given a shape configuration, we use those methods to estimate both the size of the loss region (by applying some specific criterion designed for a general triaxial system) and the size of the loss wedge (by applying some specific criterion designed for an axisymmetric system). The stars in the loss wedge and in the loss region both contribute to the stellar reservoir to be consumed by the MBH, and we obtain the draining rate  $F^{\text{drain}}$  by the maximum of their contributions in Section 4.

The stellar consumption rate contributed by the effects of both two-body relaxation and orbital precession in a non-spherical system can be set by  $F^{\text{consp}}(\mathcal{E}) \equiv \max(F^{\text{drain}}(\mathcal{E}), F_{\text{tri}}^{\text{lc}}(\mathcal{E}), F^{\text{lw}}(\mathcal{E}))$ .

### 3. DISTRIBUTIONS OF STELLAR CONSUMPTION RATES AND GALAXY/MBH DEMOGRAPHY

#### 3.1. Distributions of stellar consumption rates

We define the energy-integrated stellar consumption rate by  $\mathcal{F} \equiv \int F(\mathcal{E})d\mathcal{E}$ , which can be expressed as  $\mathcal{F}^{\text{lc}}$  (with  $F^{\text{lc}}$ ) to represent the rate contributed by two-body relaxation in a spherical potential or  $\mathcal{F}^{\text{consp}}$  (with  $F^{\text{consp}}$ ) to represent the rate contributed by both two-body relaxation and orbital precession in non-spherical potentials. We define the distribution of the stellar consumption rates by  $\Phi_{\mathcal{F}}(\mathcal{F}, M_{\text{BH}}, z)$  so that  $\Phi_{\mathcal{F}}(\mathcal{F}, M_{\text{BH}}, z)d\mathcal{F}dM_{\text{BH}}$  represents the comoving number density of MBHs at redshift  $z$  with mass within the range  $M_{\text{BH}} \rightarrow M_{\text{BH}} + dM_{\text{BH}}$  and with stellar consumption rate within the range  $\mathcal{F} \rightarrow \mathcal{F} + d\mathcal{F}$ . We define the galaxy stellar mass function  $n_{\text{gal}}(M_{\text{gal}}, z)$  so that  $n_{\text{gal}}(M_{\text{gal}}, z)dM_{\text{gal}}$  represents the comoving number density of galaxies at redshift  $z$  with mass in the range  $M_{\text{gal}} \rightarrow M_{\text{gal}} + dM_{\text{gal}}$ . Similarly, we define the mass function of the spheroidal components of galaxies (i.e., early-type galaxies and the bulge of late-type galaxies, which are both called ‘‘bulges’’ for simplicity in this work)  $n_*(M_*, z)$  so that  $n_*(M_*, z)dM_*$  represents the comoving number density of galaxies at redshift  $z$  with bulge mass in the range  $M_* \rightarrow M_* + dM_*$ . The distribution of the stellar consumption rate can be given as follows:

$$\Phi_{\mathcal{F}}(\mathcal{F}, M_{\text{BH}}, z) = \int dM_* n_*(M_*, z) p_{\text{BH}}(M_{\text{BH}}|M_*, z) \times p_{\mathcal{F}}(\mathcal{F}|M_*, M_{\text{BH}}, z) \quad (11)$$

and

$$n_*(M_*, z) = \int dM_{\text{gal}} n_{\text{gal}}(M_{\text{gal}}, z) p_*(M_*|M_{\text{gal}}, z), \quad (12)$$

where  $p_{\mathcal{F}}(\mathcal{F}|M_*, M_{\text{BH}}, z)$  is a probability function defined so that  $p_{\mathcal{F}}(\mathcal{F}|M_*, M_{\text{BH}}, z)d\mathcal{F}$  represents the probability that a bulge with mass  $M_*$  at redshift  $z$  containing an MBH with mass  $M_{\text{BH}}$  has stellar consumption rate within the range  $\mathcal{F} \rightarrow \mathcal{F} + d\mathcal{F}$ ,  $p_{\text{BH}}(M_{\text{BH}}|M_*, z)$  is a probability function defined so that  $p_{\text{BH}}(M_{\text{BH}}|M_*, z)dM_{\text{BH}}$  represents the probability that a bulge with mass  $M_*$  at redshift  $z$  contains an MBH with mass in the range  $M_{\text{BH}} \rightarrow M_{\text{BH}} + dM_{\text{BH}}$ , and  $p_*(M_*|M_{\text{gal}}, z)$  is also a probability function defined so that  $p_*(M_*|M_{\text{gal}}, z)dM_*$  represents the probability that a galaxy with mass  $M_{\text{gal}}$  at redshift  $z$  contains a bulge with mass in the range  $M_* \rightarrow M_* + dM_*$ . We have  $\int p_{\mathcal{F}}(\mathcal{F}|M_*, M_{\text{BH}}, z)d\mathcal{F} = 1$ ,  $\int p_{\text{BH}}(M_{\text{BH}}|M_*, z)dM_{\text{BH}} = 1$ , and  $\int p_*(M_*|M_{\text{gal}}, z)dM_* = 1$ . The distributions of  $p_{\text{BH}}$  and  $p_*$  depend on BH demography and galaxy demography, and the distribution of  $p_{\mathcal{F}}$  depends on the distributions of the intrinsic structure of galaxies.

The stellar consumption rate  $\mathcal{F}$  is a function of the parameters describing the mass density distribution and the shape distribution of host galaxies. The mass density distribution and the shape distribution of host galaxies are likely to evolve with redshifts. In this work, we assume that they do not evolve with redshift for simplicity. Thus,  $p_{\mathcal{F}}$  is independent of redshift  $z$ , i.e.,  $p_{\mathcal{F}}(\mathcal{F}|M_*, M_{\text{BH}}, z) = p_{\mathcal{F}}(\mathcal{F}|M_*, M_{\text{BH}})$ . When the redshift evolution information of the mass density distribution and the shape distribution is available with future observations,  $p_{\mathcal{F}}$  can be updated accordingly.

In a galaxy sample, suppose that there are  $N$  galaxies with bulge mass and MBH mass  $(M_*, M_{\text{BH}})$  that have the stellar consumption rate  $\mathcal{F}_{i|M_*, M_{\text{BH}}}$ , ( $i = 1, 2, \dots, N$ ) (with  $T$  being set to the Hubble time at the corresponding redshift in Eq. 9 for the draining in the non-spherical case). The probability function  $p_{\mathcal{F}}$  can be determined through

$$\begin{aligned} p_{\mathcal{F}}(\mathcal{F}|M_*, M_{\text{BH}}) &= \frac{1}{N} \sum_{i=1}^N \delta(\mathcal{F} - \mathcal{F}_{i|M_*, M_{\text{BH}}}) \\ &= \frac{1}{N} \frac{d}{d\mathcal{F}} \sum_{i=1}^N H(\mathcal{F} - \mathcal{F}_{i|M_*, M_{\text{BH}}}), \end{aligned} \quad (13)$$

where  $H(x)$  is a step function defined by  $H(x) = 1$  if  $x > 0$  and  $H(x) = 0$  if  $x \leq 0$ . Applying Equation (13) into Equation (11), we have

$$\begin{aligned} \Phi_{\mathcal{F}}(\mathcal{F}, M_{\text{BH}}, z) &= \frac{d}{d\mathcal{F}} \int dM_* [n_*(M_*, z) p_{\text{BH}}(M_{\text{BH}}|M_*, z) \\ &\quad \times \frac{1}{N} \sum_{i=1}^N H(\mathcal{F} - \mathcal{F}_{i|M_*, M_{\text{BH}}})]. \end{aligned} \quad (14)$$

We define an enhancement factor  $f_{\text{enhance}}$  to characterize the enhancement in the average stellar consumption rate due to both two-body relaxation and orbital precession in non-spherical potentials as compared to the rate due to two-body relaxation in spherical potentials as follows:

$$f_{\text{enhance}}(M_{\text{BH}}, z) \equiv \frac{\langle \mathcal{F}^{\text{consp}} \rangle(M_{\text{BH}}, z)}{\langle \mathcal{F}^{\text{lc}} \rangle(M_{\text{BH}}, z)}, \quad (15)$$

where the expectation of the consumption rate  $\langle \mathcal{F} \rangle$  for MBHs with mass  $M_{\text{BH}}$  at redshift  $z$  is defined by

$$\langle \mathcal{F} \rangle(M_{\text{BH}}, z) \equiv \frac{\int \mathcal{F} \Phi_{\mathcal{F}}(\mathcal{F}, M_{\text{BH}}, z) d\mathcal{F}}{\int \Phi_{\mathcal{F}}(\mathcal{F}, M_{\text{BH}}, z) d\mathcal{F}}. \quad (16)$$

We define the differential volumetric consumption rate over MBH mass  $M_{\text{BH}}$  at redshift  $z$  by

$$\frac{d\mathbb{F}_{\text{vol}}(M_{\text{BH}}, z)}{d \log M_{\text{BH}}} \equiv (M_{\text{BH}} \ln 10) \int \mathcal{F} \Phi_{\mathcal{F}}(\mathcal{F}, M_{\text{BH}}, z) d\mathcal{F}, \quad (17)$$

where  $\mathbb{F}_{\text{vol}}(M_{\text{BH}}, z)$  is the integrated volumetric consumption rate over a range of MBH mass lower than  $M_{\text{BH}}$  at redshift  $z$ .

Note that it is straightforward to generalize the above framework to define the stellar consumption rate as a function of galaxy mass  $M_{\text{gal}}$ , instead of  $M_{\text{BH}}$ . In Section 4, we will present the volumetric stellar consumption rates not only as a function of  $M_{\text{BH}}$ , but also as a function of  $M_{\text{gal}}$  (with omitting a similar formalism as above for simplicity).

### 3.2. Galaxy/MBH demography

We summarize the galaxy samples, the distributions of galaxy properties, and the MBH demography to be used in this work below, which share many similarities to those developed in CYL20, as mentioned in Section 1.

To model the statistical distributions of stellar consumption rates, we use the observational samples of early-type galaxies in the ATLAS<sup>3D</sup> survey (Cappellari et al. 2011) and those in Lauer et al. (2007) to generate a mock galaxy sample with a large size of  $\sim 10^7$  galaxies, as described in Sections 4.1 and 4.2 in CYL20). Each galaxy in the mock sample is characterized by its generated surface brightness profile and mass-to-light ratio. The mock galaxy sample with the large size covers a sufficiently large variety in galaxy properties. Note that one important parameter to characterize the inner stellar distribution of a galaxy is the inner slope  $\gamma$  in the surface brightness profile of a galaxy ( $I(R) \propto R^{-\gamma}$  as  $R \rightarrow 0$ ; see Eq. 38 in CYL20), and one of our results shown in Section 4 is to investigate the dependence on  $\gamma$ .

Note that by constructing the mock galaxy sample based on the observational galaxy samples above, we have implicitly assumed that the distribution of the combined observational galaxy sample is representative of the distribution of the galaxies in the real universe in the parameter space of the five Nuker-law parameters and the mass-to-light ratio.

Regarding the intrinsic triaxial shape distributions of galaxies, we use the observational results summarized

from the ATLAS<sup>3D</sup> survey and the Sloan Digital Sky Survey. The triaxial shape of a galaxy in the mock sample is generated randomly from the observational galaxy triaxiality distributions presented in Padilla & Strauss (2008) and Weijmans et al. (2014) (See more details in Fig. 2 and Section 4.1 in CYL20). Compared to the shape configurations shown in Padilla & Strauss (2008), those shown in Weijmans et al. (2014) are relatively closer to axisymmetric. In this work, the results are obtained with both of the shape configurations for comparison.

The galaxy stellar mass function  $n_{\text{gal}}(M_{\text{gal}}, z)$  used in this work is obtained from Behroozi et al. (2019) (see Figure 3 and Section 4.3.1 in CYL20). The probability function of  $p_{\text{BH}}$  in Equation (11) can be set through the BH–bulge relations obtained from different works in the literature (see more details in Eq. 46, Figure 5, Table 1, and Section 4.4 in CYL20). The probability function of  $p_*$  in Equation (12) is set through galaxy demography on the fractions of different types of galaxies (Behroozi et al. 2019) and their bulge-to-total stellar mass ratios (see more details in Section 4.4 in CYL20).

### 3.3. The stellar consumption rate library and its application

To evaluate the distributions of the stellar consumption rate statistically (see Eq. 11), we construct a consumption rate library based on the mock galaxy sample. In the library, we set the MBH mass so that  $\log(M_{\text{BH}}/M_{\odot})$  is in the range from 5 to 10 with an interval of 0.2. For each MBH mass considered, we select 500,000 galaxies randomly from the mock galaxy sample. Then based on the description in Section 2, the stellar distribution in each galaxy is modeled, and the stellar consumption rates  $\mathcal{F}^{\text{lc}}$  and  $\mathcal{F}^{\text{consp}}$  are estimated.

The stellar consumption rate library is then utilized to obtain the distributions of the stellar consumption rates in the realistic universe (see Eq. 14) by a Monte-Carlo method. We evaluate the distribution function of  $\Phi_{\mathcal{F}}(\mathcal{F}, M_{\text{BH}}, z)$  at the mesh points of  $\log(M_{\text{BH}}/M_{\odot})$  (in the range from 5 to 10 with an interval of 0.2), same as the mesh points in the stellar consumption rate library. For each given MBH mass, we set the integration range of  $\log(M_{\text{gal}}/M_{\odot})$  to be within [7, 13] in Equation (12), and divide the integration range into 60 bins with an interval  $\Delta \log M_{\text{gal}} = 0.1$ . Within each integration bin, we generate 2000 galaxies based on the stellar mass function  $n_{\text{gal}}(M_{\text{gal}}, z)$ . For each of the 2000 galaxies, we generate its bulge mass  $M_*$ , based on the probability

distribution of  $p_*$ . For each galaxy (e.g., denoted by  $i$ ) characterized by  $(M_*, M_{\text{BH}})$  in a bin, we search the stellar consumption rate library to find out the system with the same MBH mass  $M_{\text{BH}}$  and with the bulge mass being closest to  $M_*$ , and then assign its stellar consumption rate in the library to galaxy  $i$  generated in the bin, denoted by  $\mathcal{F}_i$ . In this way, the distributions of the stellar consumption rates are evaluated by the sum over all the galaxy mass bins, by using Equations (11)–(14).

## 4. RESULTS

In this section, we show the simulation results on how the rates of stellar consumption by central MBHs are affected by the inclusion of the loss-region draining in non-spherical potentials, and how they depend on MBH masses and inner stellar distributions of the host galaxies. We also present the differential and the integrated volumetric consumption rates at different MBH masses, different redshifts, and different galaxy masses. Some detailed results are illustrated by Figures 1–9, where the MBHs are assumed to be Schwarzschild BHs, and  $m_*$  and  $r_*$  are set to be the solar mass and radius. The results are obtained by using the MBH mass versus the galaxy bulge mass relation of Kormendy & Ho (2013); i.e., “KH13b” in Table 1 of CYL20. In Figures 6–9, we also present the median of the results obtained with all the different BH–host galaxy relations listed in Table 1 of CYL20 and the standard deviations around the median.

### 4.1. Stellar consumption rates per galaxy

Figure 1 plots the distributions of the (per-galaxy) stellar consumption rates by central MBHs (see Eq. 11), and their dependence on different MBH masses, different mechanisms of refilling stars into the loss cone, and different adopted galaxy shape distributions. We only show the distributions for the MBH population at redshift  $z = 0$ . The distributions at other redshifts have different magnitudes, proportional to the number densities of the MBHs at the corresponding redshifts. In each panel, the distributions shown by the dashed curves represent the cases in which the loss-cone refilling is due to two-body relaxation, while the distributions shown by the solid curves represent the cases in which the loss-cone refilling is due to the combined effects of two-body relaxation and orbital precession in triaxial galaxy potentials. The offsets between the two sets of distributions reveal the enhancement in the estimated stellar consumption rates caused by considering the draining

of the loss region in non-spherical galaxies. As seen from the figure, the peaks of the distributions of  $\mathcal{F}^{\text{lc}}$  (dashed lines) shift toward lower  $\mathcal{F}^{\text{lc}}$  values with increasing  $M_{\text{BH}}$ . In contrast, the peaks of the distributions of  $\mathcal{F}^{\text{consp}}$  (solid curves) shift toward higher values of  $\mathcal{F}^{\text{consp}}$  (from  $\sim 10^{-4}$  to  $\sim 3 \times 10^{-3} \text{yr}^{-1} \text{gal}^{-1}$ ) with increasing  $M_{\text{BH}}$  from  $10^7 M_{\odot}$  to  $10^9 M_{\odot}$ . In Table 1, we list the values of  $\log[\mathcal{F}/(\text{yr}^{-1} \text{gal}^{-1})]$  at the peaks of the distributions, as well as the logarithms of the mean values of  $\mathcal{F}$ . The average stellar consumption rates of  $\mathcal{F}^{\text{lc}}$  (due to two-body relaxation) have a negative correlation with MBH masses  $M_{\text{BH}}$  (as low-mass MBHs tend to be located in galaxies with steeper inner slopes; see also Fig. 2). The average stellar consumption rates of  $\mathcal{F}^{\text{consp}}$  (including the effects of triaxial galaxy shapes) range from  $\sim 5 \times 10^{-4}$  to  $\sim 6 \times 10^{-3} \text{yr}^{-1} \text{gal}^{-1}$ , and have a negative correlation with  $M_{\text{BH}}$  for  $M_{\text{BH}} \lesssim 10^7 M_{\odot}$  but a positive correlation for higher masses due to the effects of triaxial galaxy shapes. For smaller MBHs  $M_{\text{BH}} \sim 10^5\text{--}10^7 M_{\odot}$ , the offset between the peak locations of the solid and the dashed curves is  $\sim 0.5$  dex along the horizontal axis. For MBH mass  $M_{\text{BH}} \simeq 10^8 M_{\odot}$ , the offset in the peak locations can be more than one order of magnitude if the triaxial galaxy shape distribution of Padilla & Strauss (2008) is adopted (left panel). The offset is slightly smaller but still considerable if the galaxy shape distribution of Weijmans et al. (2014), which prefers axisymmetric configurations, is adopted (right panel). For MBHs with even higher masses, the offset becomes larger. The rates contribute little to the observable flare rates of tidal disruptions if the high-mass MBHs are Schwarzschild BHs, as most of the stars may be swallowed whole by the MBHs. However, if the MBHs are extremely spinning Kerr BHs, stars can still be tidally disrupted due to general relativistic effects (e.g., Kesden 2012; Mummery & Balbus 2020), and the figure suggests that the triaxial galaxy shapes are effective in increasing the stellar tidal disruption rates, especially for high-mass MBHs ( $M_{\text{BH}} \sim 10^8\text{--}10^9 M_{\odot}$ ).

We investigate the role played by the inner stellar distribution of a galaxy in regulating the stellar consumption rates and show the results in Figure 2. As mentioned in Section 3.2, one important parameter to characterize the inner stellar distribution of a galaxy is the inner slope  $\gamma$  in the surface brightness profile of a galaxy. We divide the host galaxies into “core” galaxies with  $\gamma \leq 0.5$  and “cusp” galaxies with  $\gamma > 0.5$ , and show their relative contributions to the total stellar consumption rate distributions by the solid and the dashed curves, respectively. The relative contributions shown in Figure 2 are defined by the ratios of  $\frac{(\ln 10) \mathcal{F} \Phi_{\mathcal{F}}(\mathcal{F}, M_{\text{BH}}, z=0)|_{\gamma \leq 0.5}}{\int \Phi_{\mathcal{F}}(\mathcal{F}, M_{\text{BH}}, z=0) d\mathcal{F}}$

(solid curves) and  $\frac{(\ln 10) \mathcal{F} \Phi_{\mathcal{F}}(\mathcal{F}, M_{\text{BH}}, z=0)|_{\gamma > 0.5}}{\int \Phi_{\mathcal{F}}(\mathcal{F}, M_{\text{BH}}, z=0) d\mathcal{F}}$  (dashed curves), where  $\mathcal{F}$  is  $\mathcal{F}^{\text{lc}}$  in the left panel and is  $\mathcal{F}^{\text{consp}}$  in the right panel. The results shown in Figure 2 are obtained by adopting the galaxy shape distribution of Padilla & Strauss (2008), and adoption of the shape distribution of Weijmans et al. (2014) reveals a similar trend. As seen from the peak locations and the shapes of the curves in the left panel, the average rates of stellar consumptions due to two-body relaxation are higher in the galaxies with steeper inner slopes, especially for low-mass MBHs. In the right panel, the average stellar consumption rates are also higher in galaxies with high  $\gamma$  for  $M_{\text{BH}} \sim 10^5\text{--}10^7 M_{\odot}$ . For MBHs with higher masses, the difference in the peak locations of the distributions of core galaxies and cusp galaxies becomes negligible.

Figure 3 shows both the mean stellar consumption rate due to two-body relaxation ( $\langle \mathcal{F}^{\text{lc}} \rangle$ ) (open squares) and the mean consumption rate due to triaxial galaxy shapes ( $\langle \mathcal{F}^{\text{consp}} \rangle$ ) (filled squares; lower panels) as a function of  $M_{\text{BH}}$  (left panels) and  $\gamma$  (right panels). To get the relation of  $\langle \mathcal{F}^{\text{lc}} \rangle$  or  $\langle \mathcal{F}^{\text{consp}} \rangle$  with  $\gamma$ , we calculate the distributions of stellar consumption rates in galaxies with different  $\gamma$  ranges from 0 to 1 with an interval of 0.1, similarly as done for the distributions of core/cusp galaxies in Figure 2 (but with the above different  $\gamma$  range cuts). In the left panels, we also show the results of some previous works for comparison, i.e., the result obtained based on the singular isothermal sphere model of Wang & Merritt (2004) by applying the  $M_{\text{BH}}\text{--}\sigma$  relation of Merritt & Ferrarese (2001) (blue solid line) or the  $M_{\text{BH}}\text{--}\sigma$  relation of McConnell & Ma (2013) (blue dashed line), the fitting result of Stone & Metzger (2016) in which the MBHs follow the  $M_{\text{BH}}\text{--}\sigma$  relation of McConnell & Ma (2013) (orange solid line), and the fitting result of Pfister et al. (2020) to their mock galaxy sample (green solid line). In the right panels, we also show the fitting result of Stone & Metzger (2016) to their full galaxy sample (black solid line), to their subsample with MBH masses below the mass criterion for tidal disruption of (solar-type) stars (black dotted line), and to that with MBH masses above the mass criterion (black dashed line), respectively. As seen from the upper panels, the amplitude of our mean stellar consumption rate due to two-body relaxation ( $\langle \mathcal{F}^{\text{lc}} \rangle$ ) in spherical potentials is well consistent with that of Stone & Metzger (2016), as their galaxy sample from Lauer et al. (2007) is one part of our observational sample used to generate the mock galaxy sample. In our work,  $\langle \mathcal{F}^{\text{lc}} \rangle$  has a negative correlation with  $M_{\text{BH}}$ , consistent with most of the previous works (e.g., see Wang & Merritt 2004; Stone & Metzger 2016; Kochanek 2016; Pfister et al. 2020).



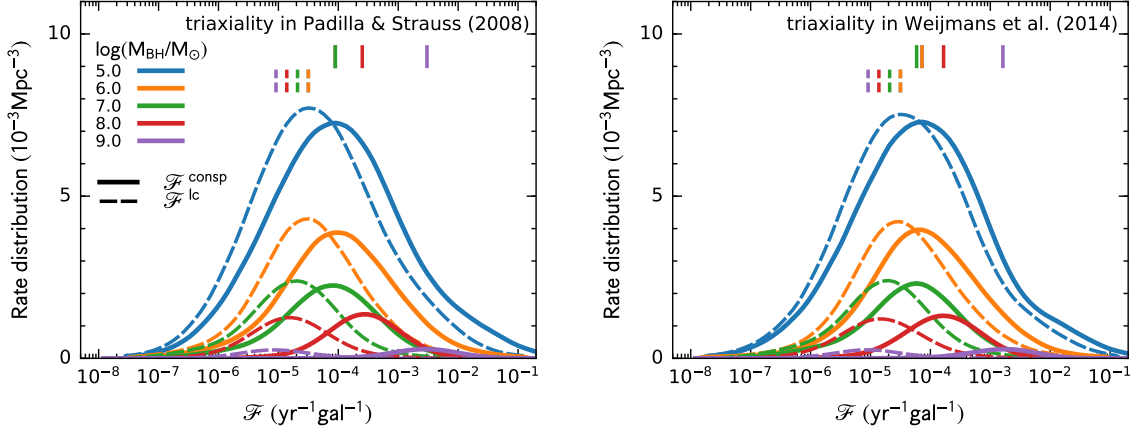


**Figure 1.** Rate distributions of stellar consumption by MBHs (see Eq. 11),  $\mathcal{F} M_{\text{BH}} (\ln 10)^2 \Phi_{\mathcal{F}}(\mathcal{F}, M_{\text{BH}}, z=0)$ , and their dependence on MBH masses and galaxy shape distributions, where  $\mathcal{F}$  is  $\mathcal{F}^{\text{lc}}$  (dashed line; due to two-body relaxation) or  $\mathcal{F}^{\text{consp}}$  (solid line; due to the effects of non-spherical galaxy shapes). The different colors represent different MBH masses, and the peak position of each distribution is marked by a vertical short line with its corresponding color and line style. In the left panel, the galaxy shape distribution of Padilla & Strauss (2008) is adopted; and in the right panel, the galaxy shape distribution of Weijmans et al. (2014) is adopted. As seen from the figure, given an MBH mass, the  $\mathcal{F}^{\text{consp}}$  value at the peak location is larger than the corresponding  $\mathcal{F}^{\text{lc}}$  value at the peak location. The  $\mathcal{F}^{\text{lc}}$  peak value shifts leftward with increasing MBH masses  $M_{\text{BH}}$ , while the  $\mathcal{F}^{\text{consp}}$  peak value shifts rightward with increasing MBH masses  $M_{\text{BH}}$  from  $10^7 M_{\odot}$  to higher masses. The offsets between the distributions of  $\mathcal{F}^{\text{lc}}$  and the  $\mathcal{F}^{\text{consp}}$  increase with increasing MBH masses. For  $M_{\text{BH}} \sim 10^5\text{--}10^6 M_{\odot}$ , the offset between the  $\mathcal{F}^{\text{lc}}$  and  $\mathcal{F}^{\text{consp}}$  peak values is  $\sim$  a factor of 3; and it becomes more than one order of magnitude for  $M_{\text{BH}} \simeq 10^8 M_{\odot}$ . Compared to the offsets shown in the left panel, those in the right panel are only slightly smaller, which indicates that the loss-region draining (obtained with galaxy shape configurations close to being axisymmetric in Weijmans et al. (2014)) is only slightly less effective. The large offsets for high-mass MBHs ( $M_{\text{BH}} \sim 10^8\text{--}10^9 M_{\odot}$ ) suggest that triaxial galaxy shapes are effective in increasing the rates of stellar tidal disruption by the high-mass MBHs if the MBHs are extremely spinning Kerr BHs or increasing the rates of stars swallowed by the MBHs if the MBHs are Schwarzschild BHs. See Section 4.

**Table 1.** The peak and the mean (per-galaxy) stellar consumption rates.

$\log(M_{\text{BH}}/M_{\odot})$	$\log \mathcal{F}^{\text{lc}} _{\text{peak}}$	$\log \langle \mathcal{F}^{\text{lc}} \rangle$	Padilla & Strauss (2008)		Weijmans et al. (2014)	
			$\log \mathcal{F}^{\text{consp}} _{\text{peak}}$	$\log \langle \mathcal{F}^{\text{consp}} \rangle$	$\log \mathcal{F}^{\text{consp}} _{\text{peak}}$	$\log \langle \mathcal{F}^{\text{consp}} \rangle$
5.0	-4.50	-3.03	-4.05	-2.55	-4.14	-2.66
6.0	-4.50	-3.51	-4.05	-2.94	-4.14	-3.10
7.0	-4.68	-3.97	-4.05	-3.33	-4.23	-3.59
8.0	-4.86	-4.21	-3.60	-3.15	-3.78	-3.41
9.0	-5.04	-4.54	-2.52	-2.25	-2.79	-2.53

NOTE—The peak and the mean values of the stellar consumption rates for the distributions shown in Figure 1. The stellar consumption rate  $\mathcal{F}$  is in units of  $\text{yr}^{-1} \text{gal}^{-1}$ . The results obtained by applying the galaxy triaxiality distributions from Padilla & Strauss (2008) and Weijmans et al. (2014) are both listed in the table.

As can be seen from the lower panels, the inclusion of the effects of triaxial galaxy shapes not only improves the average stellar consumption rate but also changes its correlation with both  $M_{\text{BH}}$  and  $\gamma$ .

In the upper left panel of Figure 3, the slopes in the  $\log(\mathcal{F}^{\text{lc}})\text{--}\log(M_{\text{BH}})$  correlation vary among the different works, e.g., -0.25 and -0.38 for Wang & Merritt

(2004) where the  $M_{\text{BH}}\text{--}\sigma$  relations of Merritt & Ferrarese (2001) and McConnell & Ma (2013) are adopted, respectively, -0.404 for the fitting to the full galaxy sample in Stone & Metzger (2016) and -0.247/-0.223 for the fitting to their core/cusp galaxy subsamples, and -0.14 for the galaxy samples with MBH masses below the mass criterion for tidal disruption of (solar-type) stars and considering the effects of nuclear star clusters in some of

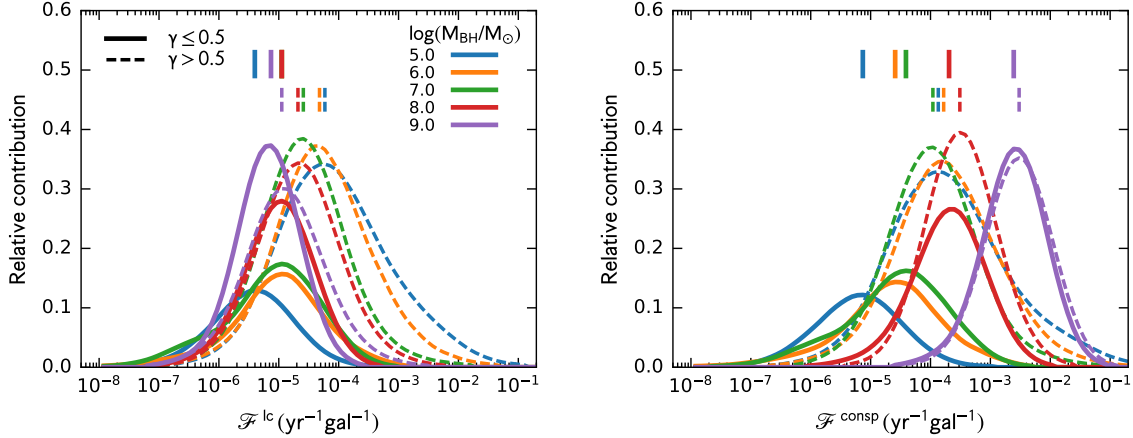


**Figure 2.** Dependence of the stellar consumption rate distributions on the inner slope of the surface brightness profiles of galaxies  $\gamma$ . The vertical axis shows the relative contributions of “core” galaxies (with  $\gamma \leq 0.5$ ; solid curves) and “cusp” galaxies ( $\gamma > 0.5$ ; dashed curves) to the distributions of the stellar consumption rate of all the galaxies, defined by  $\frac{(\ln 10) \int \Phi_{\mathcal{F}}(\mathcal{F}, M_{\text{BH}}, z=0) |_{\gamma \leq 0.5} d\mathcal{F}}{\int \Phi_{\mathcal{F}}(\mathcal{F}, M_{\text{BH}}, z=0) d\mathcal{F}}$  (solid curves) and  $\frac{(\ln 10) \int \Phi_{\mathcal{F}}(\mathcal{F}, M_{\text{BH}}, z=0) |_{\gamma > 0.5} d\mathcal{F}}{\int \Phi_{\mathcal{F}}(\mathcal{F}, M_{\text{BH}}, z=0) d\mathcal{F}}$  (dashed curves), respectively, where  $\mathcal{F}$  corresponds to  $\mathcal{F}^{\text{lc}}$  in the left panel and  $\mathcal{F}^{\text{consp}}$  in the right panel. The peak position of each curve is marked by a short vertical line with its corresponding color and line style. The galaxy shape distribution of Padilla & Strauss (2008) is adopted in this figure. As seen from the shapes and the peak locations of the curves in the left panel, the average rates of stellar consumptions due to two-body relaxation are higher in galaxies with high  $\gamma$  than those in galaxies with low  $\gamma$ , which is significant especially for low-mass MBHs (e.g.,  $M_{\text{BH}} \simeq 10^5 M_{\odot}$ ) and becomes less significant as the MBH mass increases. Similarly, the shapes and the peak locations of the distributions in the right panel (for  $\mathcal{F}^{\text{consp}}$  due to the effects of non-spherical galaxy shapes) show that the average stellar consumption rates are also significantly higher in galaxies with high  $\gamma$  for  $M_{\text{BH}} \sim 10^5$ – $10^7 M_{\odot}$ . See Section 4.

the galaxies in Pfister et al. (2020). A linear fit to the five data points obtained in our work gives a slope of  $-0.37$ . In the lower left panel, our result obtained with the inclusion of the effects of triaxial galaxy shapes shows that  $\langle \mathcal{F}^{\text{consp}} \rangle$  has a negative correlation with  $M_{\text{BH}}$  for  $M_{\text{BH}} \lesssim 10^7 M_{\odot}$ , and the correlation becomes positive for  $M_{\text{BH}} \gtrsim 10^7 M_{\odot}$ . The  $\langle \mathcal{F}^{\text{consp}} \rangle$  is larger than  $\langle \mathcal{F}^{\text{lc}} \rangle$  by a factor of  $\sim 3$  for  $10^5 \lesssim M_{\text{BH}} \lesssim 10^7 M_{\odot}$ , and by more than one and two orders of magnitude for  $M_{\text{BH}} \simeq 10^8 M_{\odot}$  and  $10^9 M_{\odot}$ , respectively.

In the upper right panel of Figure 3, our result of  $\langle \mathcal{F}^{\text{lc}} \rangle$  shows a positive correlation with  $\gamma$ , qualitatively consistent with Stone & Metzger (2016). The correlation is stronger for low MBH masses: at high  $\gamma$  (e.g.,  $\sim 1$ ),  $\langle \mathcal{F}^{\text{lc}} \rangle$  decreases with increasing  $M_{\text{BH}}$ ; and at low  $\gamma$  (e.g.,  $\sim 0$ ),  $\langle \mathcal{F}^{\text{lc}} \rangle$  first increases and then decreases with increasing  $M_{\text{BH}}$  (see also Wang & Merritt 2004 for the transition between these two trends as  $\gamma$  decreases, i.e., Figure 3 and Section 4 therein). The lower right panel shows that there exists a positive correlation between  $\langle \mathcal{F}^{\text{consp}} \rangle$  and  $\gamma$  for  $10^5 \lesssim M_{\text{BH}} \lesssim 10^7 M_{\odot}$ ; however, the correlation becomes quite weak for larger MBHs.

The dichotomy behavior of the  $\langle \mathcal{F}^{\text{consp}} \rangle$ – $M_{\text{BH}}$  and the  $\langle \mathcal{F}^{\text{consp}} \rangle$ – $\gamma$  correlations for low-mass MBHs ( $M_{\text{BH}} \lesssim 10^7 M_{\odot}$ ) and those high-mass ones ( $M_{\text{BH}} \gtrsim 10^7 M_{\odot}$ ) is

because in the two MBH mass ranges the dominant flux of stellar consumption have different origins of the stellar low-angular-momentum orbits, though the stars all move into the loss cone from the loss region. In spherical galaxies, the stellar consumption flux is dominated by stellar diffusion into the loss cone by two-body relaxation. In triaxial galaxies, stars initially inside the loss region are drained at a timescale of  $P(\mathcal{E})J_{\text{r}}^2(\mathcal{E})/J_{\text{lc}}^2(\mathcal{E})$ . Given a characteristic energy of stellar orbits (e.g., with apocenter distances being at the influential radius of an MBH), for low-mass MBHs, the stars initially inside the loss region are depleted in a relatively shorter timescale, and then the stellar consumption is dominated by the flux of the stars initially outside the loss region diffusing into the loss region due to two-body relaxation (and then precessing into the loss cone). For high-mass MBHs, stars initially inside the loss region are depleted in a relatively longer timescale, e.g., longer than a Hubble time, and the stellar consumption is dominated by the loss-region draining rate of the stars initially inside the loss region. The above different origins can serve as an explanation for the dichotomy trends from a statistical perspective, though this might not be the case in some individual systems.

Figure 4 plots the enhancement factor  $f_{\text{enhance}}(M_{\text{BH}}, z=0)$  (Eq. 15) as a function of MBH

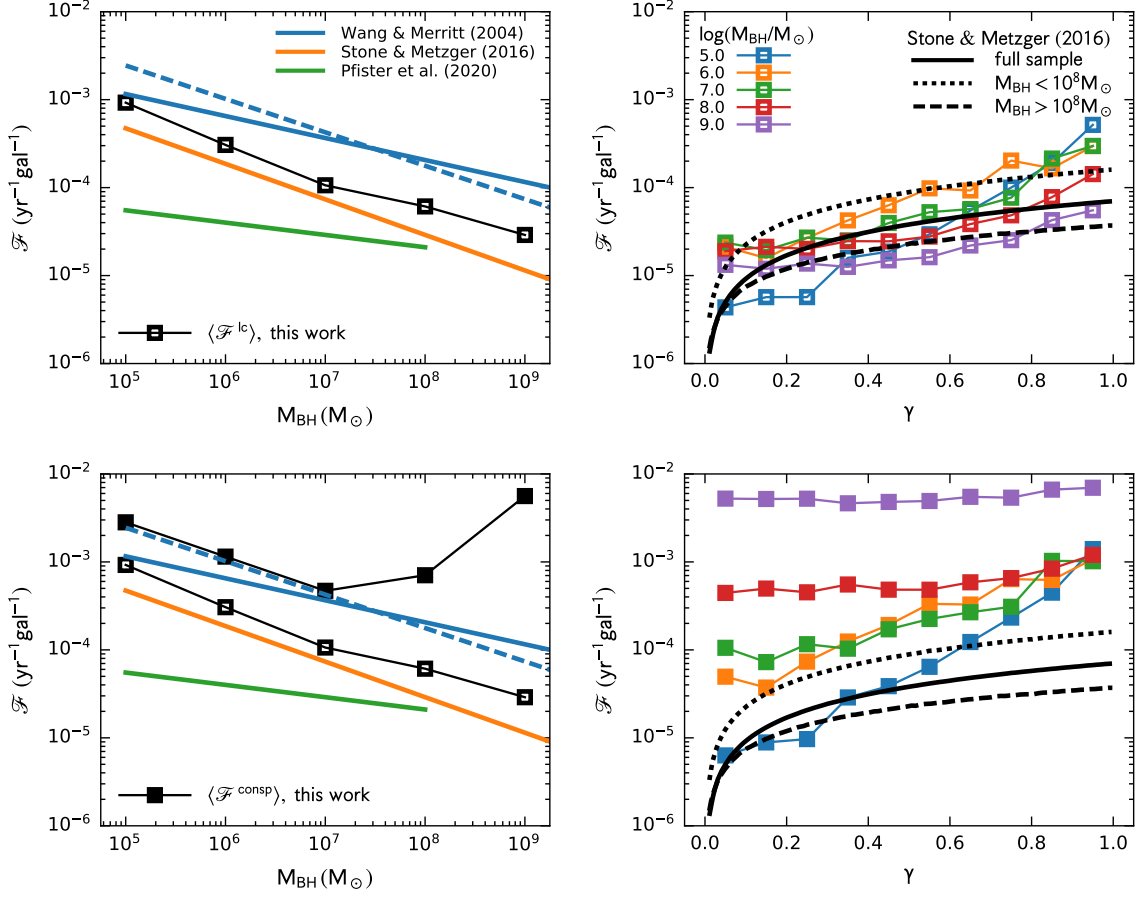


**Figure 3.** Dependence of the stellar consumption rate by MBHs  $\mathcal{F}$  on the MBH mass  $M_{\text{BH}}$  (left panels) and the inner slope of the surface brightness profile  $\gamma$  (right panels). In the upper left panel, the open squares represent the mean stellar consumption rates due to two-body relaxation ( $\langle \mathcal{F}^{\text{lc}} \rangle$ ) obtained in our study; and the other colored lines represent the results obtained in some other works, which correspond to the singular isothermal sphere model-based relation of Wang & Merritt (2004) obtained with the  $M_{\text{BH}}-\sigma$  relation of Merritt & Ferrarese (2001) (blue solid line) and with the  $M_{\text{BH}}-\sigma$  relation of McConnell & Ma (2013) (blue dashed line), the fitting result of Stone & Metzger (2016) in which the MBH masses follow the  $M_{\text{BH}}-\sigma$  relation of McConnell & Ma (2013) (orange solid line), and the fitting result of Pfister et al. (2020) to their mock galaxy sample (green solid line), respectively. In the upper right panel, the open squares represent  $\langle \mathcal{F}^{\text{lc}} \rangle$  obtained in our study, and each square represents the average rate for the host galaxies with  $\gamma$  being in some specific ranges, i.e.,  $[0.0, 0.1]$ ,  $[0.1, 0.2]$ , ..., and  $[0.9, 1.0]$ ; and the different colors represent different MBH masses. The panel also shows the fitting results of Stone & Metzger (2016) to their full galaxy sample (black solid line), to their subsample with MBH masses below the mass criterion for tidal disruption of (solar-type) stars (black dotted line), and to their subsample with MBH masses above the mass criterion (black dashed line), respectively. In the lower panels, we show the mean stellar consumption rate due to the effects of triaxial galaxy shapes,  $\langle \mathcal{F}^{\text{consp}} \rangle$ , by filled squares. As seen from the figure,  $\langle \mathcal{F}^{\text{lc}} \rangle$  correlates negatively with  $M_{\text{BH}}$ , consistent with most of the other works (e.g., Wang & Merritt 2004; Stone & Metzger 2016; Pfister et al. 2020); and it correlates positively with  $\gamma$ , and the correlation becomes stronger for low-mass MBHs. The  $\langle \mathcal{F}^{\text{consp}} \rangle$  has a negative correlation with  $M_{\text{BH}}$  for  $M_{\text{BH}} \lesssim 10^7 M_{\odot}$ , and the correlation becomes positive for  $M_{\text{BH}} \gtrsim 10^7 M_{\odot}$ . The correlation between  $\langle \mathcal{F}^{\text{consp}} \rangle$  and  $\gamma$  is positive for  $10^5 \lesssim M_{\text{BH}} \lesssim 10^7 M_{\odot}$  and becomes negligible for larger MBHs. See Section 4.

mass  $M_{\text{BH}}$ , to show the enhancement in stellar consumption rates due to the inclusion of effects of triaxial galaxy shapes. We also show  $f_{\text{enhance}}$  for core galaxies and cusp galaxies by the green and the red curves, respectively, to see how the rate enhancement is affected by the inner stellar distribution of host galaxies. As seen from the figure, the enhancement is a factor of  $\sim 3$  for MBHs with mass  $M_{\text{BH}} \lesssim 10^7 M_{\odot}$ , which is domi-

nated by stars refilling the loss region due to two-body relaxation (and then precessing into the loss cone). The enhancement factor  $f_{\text{enhance}}$  increases with the increase of MBH mass  $M_{\text{BH}}$ , and can be up to about one order of magnitude at  $M_{\text{BH}} \simeq 10^8 M_{\odot}$  and more than two orders of magnitude at  $M_{\text{BH}} \simeq 10^9 M_{\odot}$ . Compared to the results obtained by using the galaxy shape distribution of Padilla & Strauss (2008), the enhancement factor

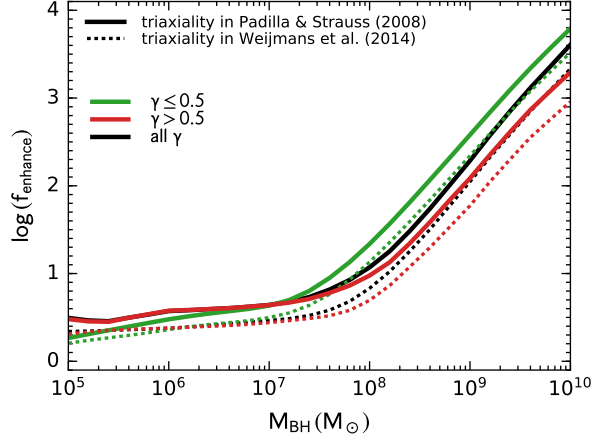
obtained by adopting the galaxy shape distribution of Weijmans et al. (2014) (which prefers axisymmetric configurations) is slightly smaller, e.g., by  $\sim 0.3$  dex at  $M_{\text{BH}} \simeq 10^8 M_{\odot}$ . For MBHs with mass greater than a few times of  $10^7 M_{\odot}$ , the enhancement in core galaxies is larger than that in cusp galaxies, as the consumption rate due to two-body relaxation in core galaxies is smaller than that in cusp galaxies (see Figure 2).

As mentioned in Section 2.2, we obtain the draining rate of a loss region at a time  $T$  that is the Hubble time of the corresponding redshift in Equation (9). However, the host galaxies may be younger, or they may have gone through multiple major mergers during their lifetime so that their distributions have been changed, or the structures with different mass scales may form at different cosmic time. To see how the stellar consumption rate in the galaxies with different lifetimes are affected by triaxial galaxy shapes, we show the enhancement factor  $f_{\text{enhance}}$  as a function of the draining time  $T$  for MBHs with different masses in Figure 5. As seen from the figure, from  $T = 1$  Gyr to the Hubble time at  $z = 0$ , the enhancement factor changes little for  $M_{\text{BH}} \sim 10^5\text{--}10^7 M_{\odot}$ , and decreases by  $\sim 0.5$  dex for  $M_{\text{BH}} \sim 10^8\text{--}10^9 M_{\odot}$ . If a galaxy formed or experienced its last major merger at  $z \sim 1$ , the enhancement factor at  $T = 8$  Gyr (the cosmic time since  $z \sim 1$ ) is higher than the enhancement factor at the Hubble time at  $z = 0$  only by  $\sim 0.2$  dex for  $M_{\text{BH}} \sim 10^8\text{--}10^9 M_{\odot}$ , and is almost the same as the enhancement factor at the  $z = 0$  Hubble time for  $M_{\text{BH}} \sim 10^5\text{--}10^7 M_{\odot}$ . Thus the statistical results of the stellar consumption rates obtained in this work (for normal galaxies) should not be affected significantly by the assumption of  $T$  being set to the Hubble time of the corresponding redshift. Note that for high-mass MBHs, though the loss-region draining rate at a given  $\mathcal{E}$  shown in Equation (9) decrease exponentially with increasing  $T$ , the mild decrease of  $f_{\text{enhance}}$  with increasing  $T$  shown in Figure 5 is a consequence of the facts that  $f_{\text{enhance}}$  is contributed by the draining rates at different  $\mathcal{E}$ , and that the draining timescales  $P(\mathcal{E})J_{\text{r}}^2(\mathcal{E})/J_{\text{c}}^2(\mathcal{E})$  are different at different  $\mathcal{E}$  (which can be longer than the relevant timescale, e.g., the Hubble timescale, for low  $\mathcal{E}$ ).

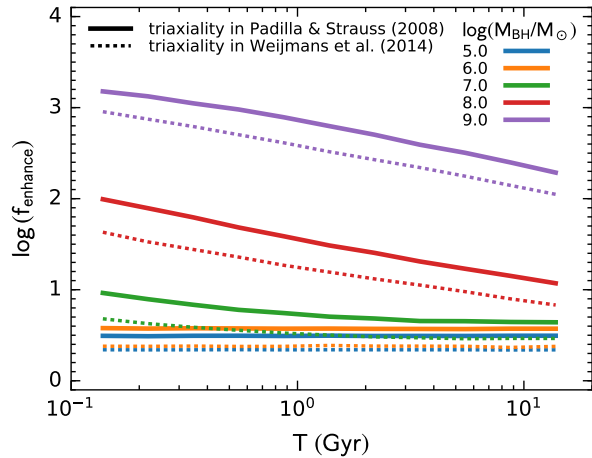
#### 4.2. Volumetric stellar consumption rates

Figure 6 plots the differential volumetric consumption rate  $d\mathbb{F}_{\text{vol}}^{\text{lc}}/d\log M_{\text{BH}}$  and  $d\mathbb{F}_{\text{vol}}^{\text{consp}}/d\log M_{\text{BH}}$  (Eq. 17) as a function of MBH mass  $M_{\text{BH}}$  at the three different redshifts  $z = 0, 2$ , and 4 (left panels) and the integrated volumetric stellar consumption rate as a func-

tion of redshift (right panels). We obtain the rates by applying the different BH–host galaxy relations (listed in Table 1 of CYL20), and for each case we show the medians of the rates in the figure (solid, dotted, dashed curves). The rates obtained with the MBH mass versus the galaxy bulge mass relation of Kormendy & Ho (2013) are shown by the dotted-dashed curves in the bottom panels, which are generally higher than the corresponding median results (solid curves) at  $M_{\text{BH}} \gtrsim 10^8 M_{\odot}$ . For the solid curves, we use the shaded region to illustrate the standard deviation of the logarithms of the rates obtained with the different BH–host galaxy relations around the medians. As seen from the figure, the volumetric stellar consumption rates decrease with increasing redshifts, and the decrease is relatively mild for  $M_{\text{BH}} \sim 10^5\text{--}10^7 M_{\odot}$  and stronger for higher  $M_{\text{BH}}$ . Note that the redshift evolution of the integrated volumetric consumption rate  $\mathbb{F}_{\text{vol}}^{\text{lc}}$  in our study is different from that of Kochanek (2016) in the detailed shape or slope of the evolution curve, though the normalizations at redshift  $z = 0$  are consistent. We find that such a difference may be caused by the MBH mass function and its redshift evolution in the two works, as the volumetric consumption rate is proportional to the MBH mass function. An improvement in determining the redshift evolution of the MBH mass function can help to reveal the redshift evolution of the stellar consumption rates, and vice versa. Consideration of the effects of triaxial galaxy shapes can cause the median volumetric stellar consumption rate to be enhanced by a factor of  $\sim 3$  for MBHs with mass  $M_{\text{BH}} \lesssim 10^7 M_{\odot}$  if the galaxy shape distribution of Padilla & Strauss (2008) is adopted. This enhancement increases to a factor of  $\sim 8$  and to two orders of magnitude at  $M_{\text{BH}} \simeq 10^8 M_{\odot}$  and  $\simeq 10^9 M_{\odot}$ , respectively. If the galaxy shape distribution of Weijmans et al. (2014) is adopted, the enhancement is slightly smaller. We list the integrated volumetric consumption rate at  $z = 0$  in Table 2. For the case of adopting the galaxy shape distribution of Padilla & Strauss (2008), the median integrated volumetric consumption rate contributed by central MBHs within the mass range of  $10^5\text{--}10^7 M_{\odot}$  due to two-body relaxation [ $\mathbb{F}_{\text{vol}}^{\text{lc}}(M_{\text{BH}} = 10^7 M_{\odot}) - \mathbb{F}_{\text{vol}}^{\text{lc}}(M_{\text{BH}} = 10^5 M_{\odot})$ ] and that obtained by considering the effect of galaxy triaxial shapes [ $\mathbb{F}_{\text{vol}}^{\text{consp}}(M_{\text{BH}} = 10^7 M_{\odot}) - \mathbb{F}_{\text{vol}}^{\text{consp}}(M_{\text{BH}} = 10^5 M_{\odot})$ ] are  $1.1 \times 10^{-5} \text{yr}^{-1} \text{Mpc}^{-3}$  and  $3.1 \times 10^{-5} \text{yr}^{-1} \text{Mpc}^{-3}$  at  $z = 0$ , respectively; the corresponding median rates contributed by MBHs within the mass range of  $10^7\text{--}10^8 M_{\odot}$  are  $3.0 \times 10^{-7} \text{yr}^{-1} \text{Mpc}^{-3}$  and  $1.4 \times 10^{-6} \text{yr}^{-1} \text{Mpc}^{-3}$ , respectively. The corresponding median rates contributed by MBHs within the mass range of  $10^8\text{--}10^9 M_{\odot}$  are  $4.0 \times 10^{-8} \text{yr}^{-1} \text{Mpc}^{-3}$  and



**Figure 4.** The enhancement factor  $f_{\text{enhance}}(M_{\text{BH}}, z = 0)$  (Eq. 15) as a function of central MBH mass  $M_{\text{BH}}$ , describing the enhancement of the stellar consumption rate due to adding the effects of triaxial galaxy shapes. The solid and the dotted curves show the results obtained by using the galaxy shape distribution of [Padilla & Strauss \(2008\)](#) and that of [Weijmans et al. \(2014\)](#), respectively. The green and the red curves correspond to the results obtained for “core” galaxies ( $\gamma \leq 0.5$ ) and “cusp” galaxies ( $\gamma > 0.5$ ), respectively, and the black curves represent the results obtained for all the “core” and “cusp” galaxies. As seen from the figure, the enhancement factor  $f_{\text{enhance}}$  increases with increasing MBH mass  $M_{\text{BH}}$ . For  $M_{\text{BH}} \lesssim 10^7 M_{\odot}$ , the increasing trend is relatively weak; when  $M_{\text{BH}} \gtrsim 10^8 M_{\odot}$ , the trend becomes much stronger. For  $M_{\text{BH}} \sim 10^5 - 10^7 M_{\odot}$ , the enhancement is a factor of  $\sim 3$  if the galaxy shape distribution of [Padilla & Strauss \(2008\)](#) is adopted; for  $M_{\text{BH}} \simeq 10^8 M_{\odot}$ , the enhancement can be about one order of magnitude. For  $M_{\text{BH}}$  higher than a few times of  $10^7 M_{\odot}$ , the enhancement is larger in core galaxies than that in cusp galaxies. The enhancement obtained by using the galaxy shape distribution of [Padilla & Strauss \(2008\)](#) is slightly larger than that obtained by using the distribution of [Weijmans et al. \(2014\)](#). See Section 4.



**Figure 5.** The enhancement factor  $f_{\text{enhance}}$  as a function of the draining time  $T$  (i.e., the time duration that the loss region has been drained; see  $T$  in Equation 9). The different colors correspond to different MBH masses. The solid and dotted curves show the results obtained by using the galaxy shape distribution of [Padilla & Strauss \(2008\)](#) and that of [Weijmans et al. \(2014\)](#), respectively. As seen from the figure,  $f_{\text{enhance}}$  decreases mildly with increasing  $T$  for MBHs with mass  $M_{\text{BH}} \sim 10^8 - 10^9 M_{\odot}$  ( $\sim 0.5$  dex from  $T \sim 1$  to  $10$  Gyr); and it is almost flat at  $T \sim 1 - 10$  Gyr for MBHs with mass  $M_{\text{BH}} \sim 10^5 - 10^7 M_{\odot}$ . The mild change of  $f_{\text{enhance}}$  with  $T$  suggests that the statistical results of the stellar consumption rates obtained in this work should not be affected significantly by the assumption of the draining time  $T$  being set to the Hubble time of the corresponding redshift. See Section 4.

$7.8 \times 10^{-7} \text{yr}^{-1} \text{Mpc}^{-3}$ , respectively; and the rate obtained with the BH–host galaxy relation in [Kormendy & Ho \(2013\)](#) can be up to  $2.0 \times 10^{-6} \text{yr}^{-1} \text{Mpc}^{-3}$ . If the MBHs with  $M_{\text{BH}} \sim 10^8 - 10^9 M_{\odot}$  are extremely spin-

ning Kerr BHs, the upper mass limit of the MBH that can tidally disrupt a star can increase from  $\sim 10^8 M_{\odot}$  to  $\sim 10^9 M_{\odot}$  (e.g., [Mummery & Balbus 2020](#); [Kesden 2012](#)), the rates of stellar disruption by those BHs can

be effectively improved by the effects of the galaxy triaxiality, which enables a significant event rate with respect to those for low-mass MBHs especially at low redshifts (e.g.,  $\sim 1\%$ – $10\%$  of the rates for low-mass MBHs).

In the left panels of Figure 6, we also plot the volumetric TDE flaring rate estimated from a recently compiled sample of TDE candidates with black hole mass measurements (van Velzen 2018), where the number of the observational sources to determine each data point is 5, 4, 2, and 1 from left to right. It appears that the observational constraints are smaller than the model predictions by a factor of up to ten or more. One may note that the sample incompleteness, or unknown selection effects and MBH occupation fractions in low-mass galaxies, or some other effects may lead to large errors in the observational constraints, which hinders a direct comparison between observations and model results (see also Stone & Metzger 2016). Accumulation of more observational sources and better understanding of various effects involved in the estimates in future will help to put constraints on the model.

Note that the MBH mass in Figures 1–4 is obtained by adopting the MBH mass versus the galaxy bulge mass relation of Kormendy & Ho (2013), which is generally higher than most of the other BH–host galaxy relations shown in Figure 5 and Table 1 of CYL20. Adoption of most of the other different BH–host galaxy relations can result in an increase of the per-galaxy stellar consumption rates. For most of the other different BH–host galaxy relations, our calculations show that the peak locations shown in Figure 1 will shift toward higher stellar consumption rates by  $\sim 0$ – $0.5$  dex, together with wider distribution shapes. As the galaxy comoving number density decreases significantly with increasing galaxy masses at the high-mass end, adoption of the other different BH–host galaxy relations results in the decrease of the volumetric stellar consumption rates for high-mass BHs ( $M_{\text{BH}} \gtrsim 10^8 M_{\odot}$ ; e.g., by a factor of a few or up to one order of magnitude), as illustrated by the comparison of the dotted-dashed curves and the solid curves in Figure 6. (See Figure 19 of CYL20 for another example of the effect caused by the scattering of the BH–host galaxy relations, in the predicted stochastic gravitational wave radiation background of cosmic supermassive binary black holes.)

In the lower left panel of Figure 6, there appears a “bump” feature in the dotted-dashed curve in the MBH mass range between a few times  $10^7 M_{\odot}$  and  $10^{10} M_{\odot}$  (obtained with the MBH mass to bulge mass relation of

Kormendy & Ho (2013)). The appearance of the bump is because within this mass range, the per-galaxy stellar consumption rate obtained with including the effects of triaxial galaxy shapes  $\mathcal{F}^{\text{consp}}$  is an increasing function of MBH mass  $M_{\text{BH}}$ , whereas the comoving number density of MBHs is a decreasing function of  $M_{\text{BH}}$ . The shape of the curve results from the combination of these two opposite trends, and the preference for a heavier MBH at a given galaxy mass set by the MBH mass to bulge mass relation of Kormendy & Ho (2013) makes the bump feature prominent.

In Figure 7, we show the differential and the integrated volumetric stellar consumption rates as a function of galaxy mass  $M_{\text{gal}}$ . As seen from figure, the estimated rates in low-mass galaxies with  $M_{\text{gal}} \lesssim 10^9 M_{\odot}$  are quite uncertain due to the scatters of the BH–host galaxy relations. The median integrated rates at  $z = 0$  are  $\sim 3 \times 10^{-5} \text{yr}^{-1} \text{Mpc}^{-3}$  over the mass range of  $M_{\text{gal}} \sim 10^8$ – $10^{10} M_{\odot}$ ,  $\sim 5 \times 10^{-6} \text{yr}^{-1} \text{Mpc}^{-3}$  over the mass range of  $M_{\text{gal}} \sim 10^{10}$ – $10^{11} M_{\odot}$ , and  $\sim 9 \times 10^{-7} \text{yr}^{-1} \text{Mpc}^{-3}$  over the mass range of  $M_{\text{gal}} \sim 10^{11}$ – $10^{12} M_{\odot}$  (see the solid curves in the right panels). The MBHs in Figure 7 is over the mass range of  $M_{\text{BH}} = 10^5$ – $10^{10} M_{\odot}$ , and the results include the rates of stars being swallowed by high-mass MBHs. To see the volumetric stellar tidal disruption rates, Figures 8–9 show the results obtained with an MBH mass cut, i.e.,  $M_{\text{BH}} \leq 10^8 M_{\odot}$  (for Schwarzschild BHs) and  $M_{\text{BH}} \leq 10^9 M_{\odot}$  (for extremely spinning Kerr BHs), respectively. In Figure 8, the stellar tidal disruption rates in bright galaxies ( $\sim 3 \times 10^{-7} \text{yr}^{-1} \text{Mpc}^{-3}$  at  $z = 0$  for  $M_{\text{gal}} \sim 10^{11} M_{\odot}$ ) are suppressed significantly, compared to the stellar consumption rates shown in Figure 7. The suppression is mainly due to the dearth of relatively low-mass central MBHs (i.e.,  $M_{\text{BH}} \lesssim 10^8 M_{\odot}$ ) in these bright galaxies. The suppression trend is also shown by Pfister et al. (2020) (see the lower panel of Figure 4 therein). However, Figure 9 shows that the volumetric stellar disruption rates in bright galaxies ( $\sim 6 \times 10^{-7} \text{yr}^{-1} \text{Mpc}^{-3}$  at  $z = 0$  for  $M_{\text{gal}} \gtrsim 10^{11} M_{\odot}$ ) are higher than those in Figure 8 and up to  $\sim 2\%$  of the stellar tidal disruption rates in all the galaxies at  $z = 0$ .

### 4.3. Stellar compact remnants

One straightforward application of the above results is to roughly estimate the rates of stellar compact remnants consumed by central MBHs, including white dwarfs, neutron stars, and stellar-mass BHs. A crucial difference of the consumption of compact remnants from the consumption of normal stars is that the tidal

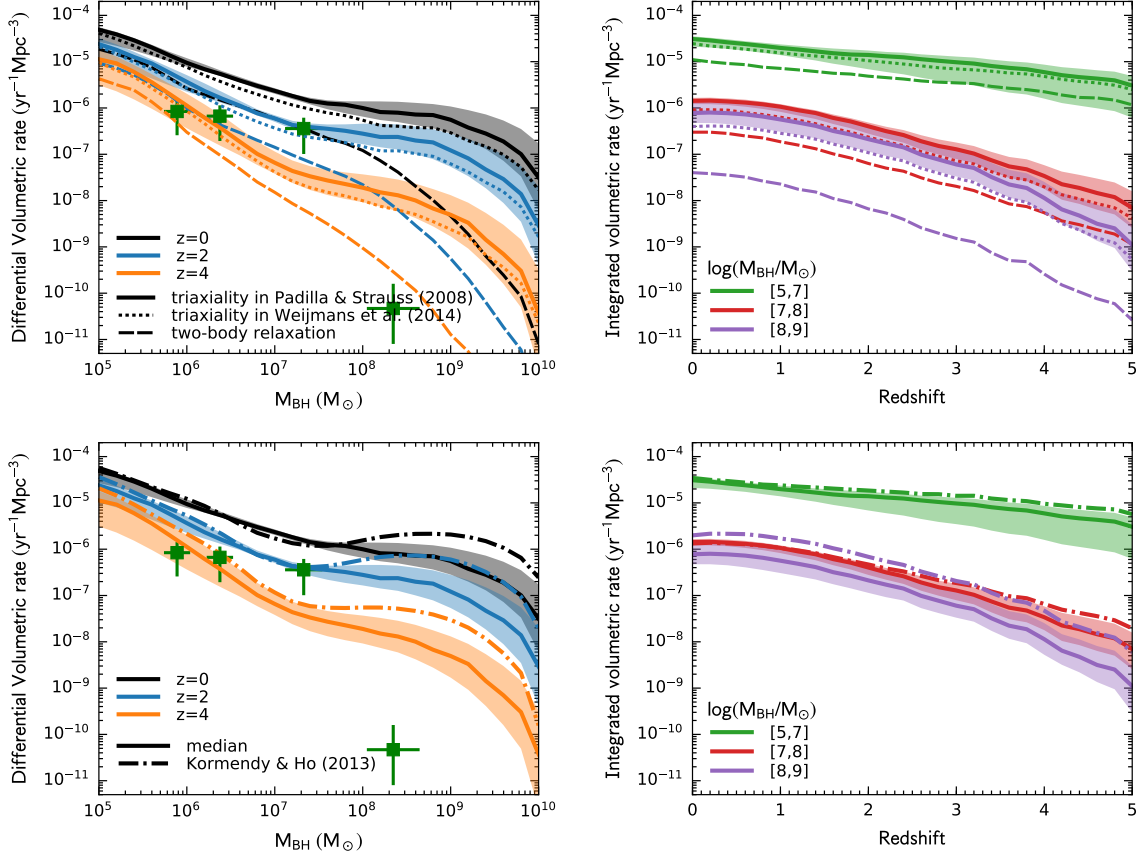


**Figure 6.** The differential volumetric stellar consumption rate as a function of MBH mass,  $d\mathbb{F}_{\text{vol}}/d\log M_{\text{BH}}(M_{\text{BH}}, z)$  (see Eq. 17; left panels) and the integrated volumetric stellar consumption rate as a function of redshift (right panels). The integrated volumetric stellar consumption rate are obtained by an integration of the differential volumetric stellar consumption rate over the ranges of  $\log(M_{\text{BH}}/M_{\odot})=[5,7]$ ,  $[7,8]$ , and  $[8,9]$ , respectively. In the upper left panel, the black, blue, and orange curves correspond to the results at redshift  $z = 0, 2$ , and  $4$ , respectively. The dashed curves represent  $d\mathbb{F}_{\text{vol}}^{\text{lc}}/d\log M_{\text{BH}}$  (upper left panel) and their integrated rates (upper right panel) due to the two-body relaxation alone, and the solid and the dotted curves represent  $d\mathbb{F}_{\text{vol}}^{\text{consp}}/d\log M_{\text{BH}}$  (left panels) and their integrated rates (right panels) obtained by adding the effects of the loss-region draining in triaxial galaxies, with the galaxy shape distributions of Padilla & Strauss (2008) and Weijmans et al. (2014), respectively. Each curve (except for the dotted-dashed curve in the bottom panels) is the median of the corresponding results obtained with the different BH-host galaxy relations listed in Table 1 of CYL20, and the shaded region around the solid curve represents the standard deviation of the logarithm of the results around the corresponding median. The dotted-dashed curves in the bottom panels represent  $d\mathbb{F}_{\text{vol}}^{\text{consp}}/d\log M_{\text{BH}}$  (bottom left panel) and their integrated rates (bottom right panel) obtained with the MBH mass versus the galaxy bulge mass relation of Kormendy & Ho (2013) and the galaxy shape distributions Padilla & Strauss (2008), for a comparison with the medians (solid curves). In the left panels, the green squares are the volumetric TDE flaring rate estimated from a recent compilation of the TDE candidates shown in Figure 10 of (van Velzen 2018), where the number of the observational sources to determine each data point is 5, 4, 2 and 1 from left to right, respectively. As seen from the upper left panel, the median  $d\mathbb{F}_{\text{vol}}^{\text{consp}}/d\log M_{\text{BH}}$  is higher than the median  $d\mathbb{F}_{\text{vol}}^{\text{lc}}/d\log M_{\text{BH}}$  by a factor of  $\sim 3$  for MBHs with mass  $M_{\text{BH}} \lesssim 10^7 M_{\odot}$  and by a factor of  $\sim 8$  at  $M_{\text{BH}} \simeq 10^8 M_{\odot}$  if the galaxy shape distribution of Padilla & Strauss (2008) is adopted. The enhancement is slightly smaller if the galaxy shape distribution of Weijmans et al. (2014) is adopted. The enhancement is about two orders of magnitude at  $M_{\text{BH}} \simeq 10^9 M_{\odot}$ . As seen from the figure, the stellar consumption rates decrease with increasing redshifts, which is relatively mild for  $M_{\text{BH}} \sim 10^5\text{--}10^7 M_{\odot}$  and stronger for higher  $M_{\text{BH}}$ . The figure suggests that the triaxial galaxy shapes are effective in increasing the stellar tidal disruption rates. See Section 4.

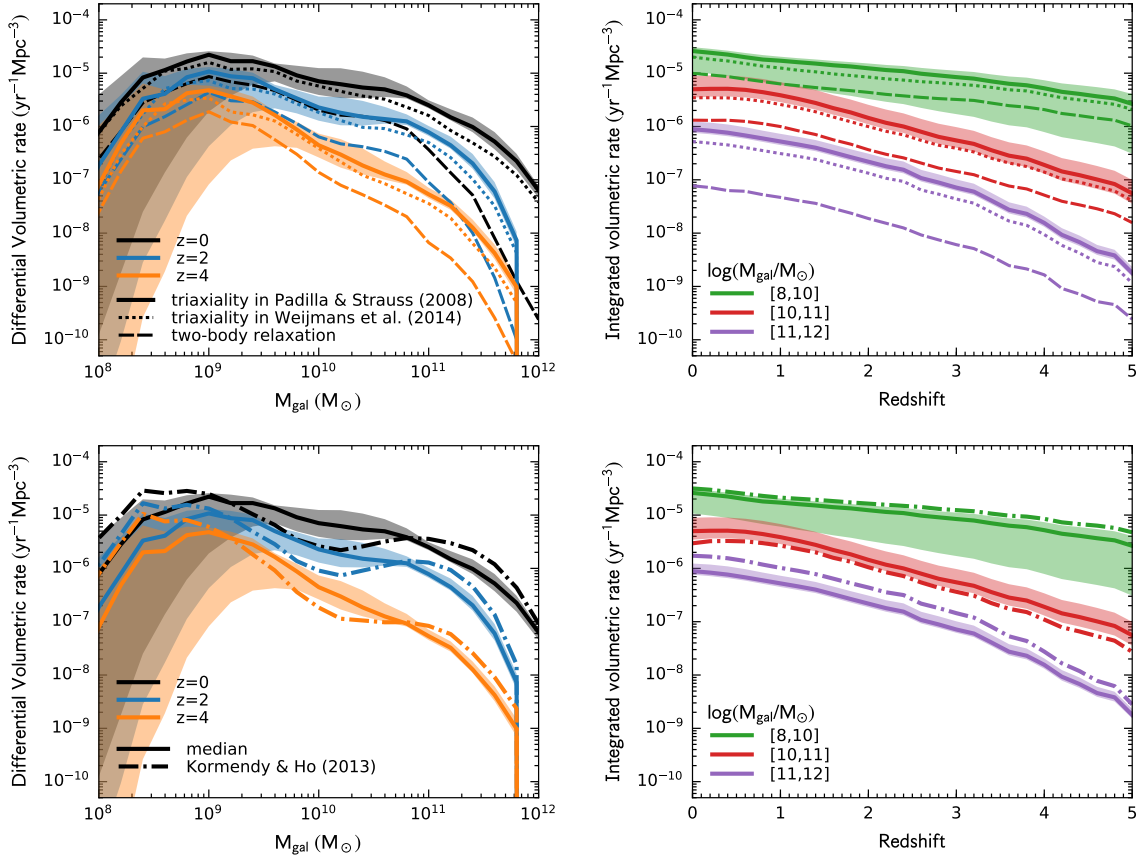
radii of compact remnants  $r_t$  are smaller than  $r_{\text{swl}} = 4GM_{\text{BH}}/c^2$  (for Schwarzschild BHs) for a wide range of  $M_{\text{BH}} = 10^5\text{--}10^{10} M_{\odot}$ , and the compact remnants in the loss cone are swallowed whole by central MBHs, with gravitational-wave bursts. The consumption rate of a

given population of compact remnants is the product of the number fraction of this population among normal stars and the stellar consumption rate (obtained by setting  $r_t = r_{\text{swl}}$ ). Here we consider three compact remnant populations: white dwarfs (WDs), neutron stars (NSs),

**Table 2.** The integrated volumetric stellar consumption rates at  $z = 0$ .

$\log(M_{\text{BH}}/M_{\odot})$	$\int \frac{dF_{\text{vol}}^{\text{lc}}}{d \log M_{\text{BH}}} d \log M_{\text{BH}}$			$\int \frac{dF_{\text{vol}}^{\text{consp}}}{d \log M_{\text{BH}}} d \log M_{\text{BH}}$			$\int \frac{dF_{\text{vol}}^{\text{consp}}}{d \log M_{\text{BH}}} d \log M_{\text{BH}}$		
				Padilla & Strauss (2008)			Weijmans et al. (2014)		
	KH13	median	stddev	KH13	median	stddev	KH13	median	stddev
[5, 7]	$1.1 \times 10^{-5}$	$1.1 \times 10^{-5}$	$^{+0.03}_{-0.11}$ dex	$3.5 \times 10^{-5}$	$3.1 \times 10^{-5}$	$^{+0.06}_{-0.17}$ dex	$2.6 \times 10^{-5}$	$2.5 \times 10^{-5}$	$^{+0.04}_{-0.18}$ dex
[7, 8]	$2.2 \times 10^{-7}$	$3.0 \times 10^{-7}$	$^{+0.04}_{-0.07}$ dex	$1.3 \times 10^{-6}$	$1.4 \times 10^{-6}$	$^{+0.06}_{-0.07}$ dex	$8.1 \times 10^{-7}$	$9.1 \times 10^{-7}$	$^{+0.05}_{-0.06}$ dex
[8, 9]	$6.7 \times 10^{-8}$	$4.0 \times 10^{-8}$	$^{+0.16}_{-0.15}$ dex	$2.0 \times 10^{-6}$	$7.8 \times 10^{-7}$	$^{+0.22}_{-0.22}$ dex	$1.1 \times 10^{-6}$	$4.0 \times 10^{-7}$	$^{+0.23}_{-0.21}$ dex

NOTE—The integrated volumetric stellar consumption rates at  $z = 0$  shown in Figure 6, in unit of  $\text{yr}^{-1}\text{Mpc}^{-3}$ . The MBH mass range of the integration is listed in the column of “ $\log(M_{\text{BH}}/M_{\odot})$ ”. The “KH13” column lists the rates obtained with the MBH mass versus the galaxy bulge mass relation of Kormendy & Ho (2013). The “median” column lists the median of the rates obtained with the different BH-host galaxy relations listed in Table 1 of CYL20; and the “stddev” column lists the standard deviation of the logarithm of the rates around the median in unit of dex. The results obtained by applying the galaxy triaxiality distributions from Padilla & Strauss (2008) and Weijmans et al. (2014) are both listed.

**Figure 7.** The volumetric stellar consumption rate as a function of galaxy stellar mass  $M_{\text{gal}}$ . The curves, colors, and texts have meanings similar to those in Figure 6, except that the rates in this figure are expressed as a function of  $M_{\text{gal}}$ , instead of  $M_{\text{BH}}$ .

and stellar-mass BHs (BHs). If their number fractions among normal stars are  $f_{\text{cr}} = 0.1, 0.01$  and  $0.001$ , respectively (e.g., see Hopman & Alexander 2005), our calculations show that their integrated volumetric consumption rates over the MBH mass ranges of  $[10^5 M_{\odot}, 10^7 M_{\odot}]$ ,

$[10^7 M_{\odot}, 10^8 M_{\odot}]$ , and  $[10^8 M_{\odot}, 10^9 M_{\odot}]$  are  $f_{\text{cr}}$  times of  $1.3 \times 10^{-5} \text{yr}^{-1} \text{Mpc}^{-3}$ ,  $1.3 \times 10^{-6} \text{yr}^{-1} \text{Mpc}^{-3}$ , and  $2.0 \times 10^{-6} \text{yr}^{-1} \text{Mpc}^{-3}$ , respectively, where the MBH-bulge mass relation of Kormendy & Ho (2013) is used. Note that the above rates can be changed due to mass



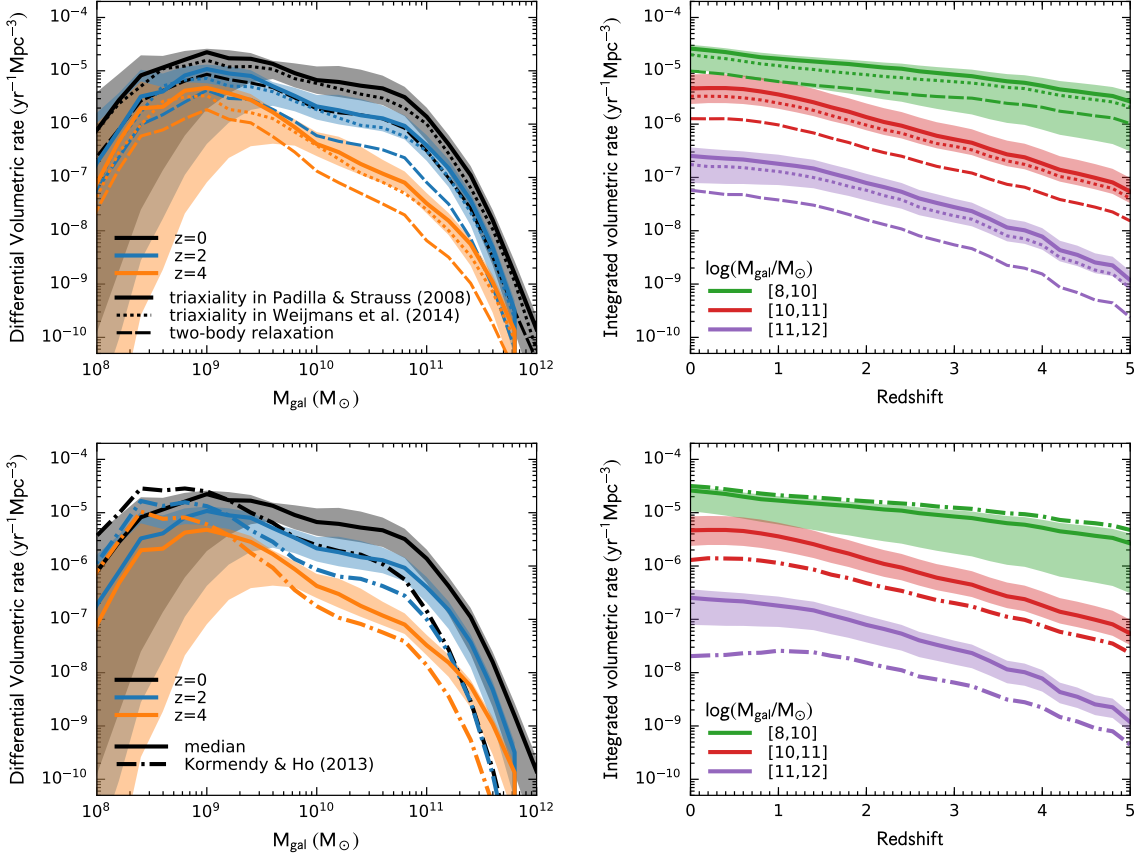


**Figure 8.** Similar to Figure 7, but excluding galaxies with MBH mass  $M_{\text{BH}} > 10^8 M_{\odot}$ . The rates in high-mass galaxies ( $M_{\text{gal}} \sim 10^{11}$ – $10^{12} M_{\odot}$ ) decrease significantly, compared to those in Figure 7. The volumetric stellar disruption rates in bright galaxies ( $\sim 3 \times 10^{-7} \text{yr}^{-1} \text{Mpc}^{-3}$  at  $z = 0$  for  $M_{\text{gal}} \gtrsim 10^{11} M_{\odot}$ ) are about 1% of the stellar tidal disruption rates in all the galaxies at  $z = 0$ .

segregation at galactic centers and any other mechanisms causing the number density distributions of compact remnants to be different from those of normal stars (e.g., see Alexander 2017).

## 5. CONCLUSIONS

We have investigated the rates of stellar consumption (either being tidally disrupted or swallowed whole) by central MBHs and their distributions in the realistic universe. By adopting observational galaxy triaxiality shape distributions and observational galaxy surface brightness distributions, we study the effects of stellar orbital precession in triaxial galaxies to enhance the number of stars that can move to the vicinity of the MBHs, as well as the effects of two-body relaxation. By incorporating the refilling rates into the loss cone and the draining rates of the loss regions in triaxial galaxies with the MBH/galaxy demography, we obtain the following main results on the distributions of both the per-galaxy and the volumetric stellar consumption rates

and their dependence on MBH and host galaxy properties.

The average (per-galaxy) stellar consumption rates in triaxial galaxies  $\mathcal{F}_{\text{consp}}$  range from  $\sim 5 \times 10^{-4} \text{yr}^{-1} \text{gal}^{-1}$  to  $\sim 6 \times 10^{-3} \text{yr}^{-1} \text{gal}^{-1}$  at  $z = 0$  and have a positive correlation with central MBH masses for  $M_{\text{BH}} \sim 10^7$ – $10^9 M_{\odot}$ , and they range from  $\sim 5 \times 10^{-4} \text{yr}^{-1} \text{gal}^{-1}$  to  $\sim 3 \times 10^{-3} \text{yr}^{-1} \text{gal}^{-1}$  at  $z = 0$  and have a negative correlation for  $M_{\text{BH}} \sim 10^5$ – $10^7 M_{\odot}$ . The rates at the peaks of the stellar consumption rate distributions increase with increasing  $M_{\text{BH}}$ , being around  $10^{-4} \text{yr}^{-1} \text{gal}^{-1}$  at  $z = 0$  for  $M_{\text{BH}} \sim 10^5$ – $10^7 M_{\odot}$  and ranging from  $\sim 3 \times 10^{-4} \text{yr}^{-1} \text{gal}^{-1}$  to  $\sim 3 \times 10^{-3} \text{yr}^{-1} \text{gal}^{-1}$  at  $z = 0$  for  $M_{\text{BH}} \sim 10^8$ – $10^9 M_{\odot}$ . The enhancement in the stellar consumption rates caused by adding the effects of galaxy triaxial shapes is by a factor of  $\sim 3$ – $5$  for  $M_{\text{BH}} \lesssim 10^7 M_{\odot}$  and increases with increasing central MBH masses, which can be up to one order of magnitude for MBHs with  $M_{\text{BH}} \sim 10^8 M_{\odot}$  and two orders of magnitude for  $M_{\text{BH}} \sim 10^9 M_{\odot}$ . The stellar consump-

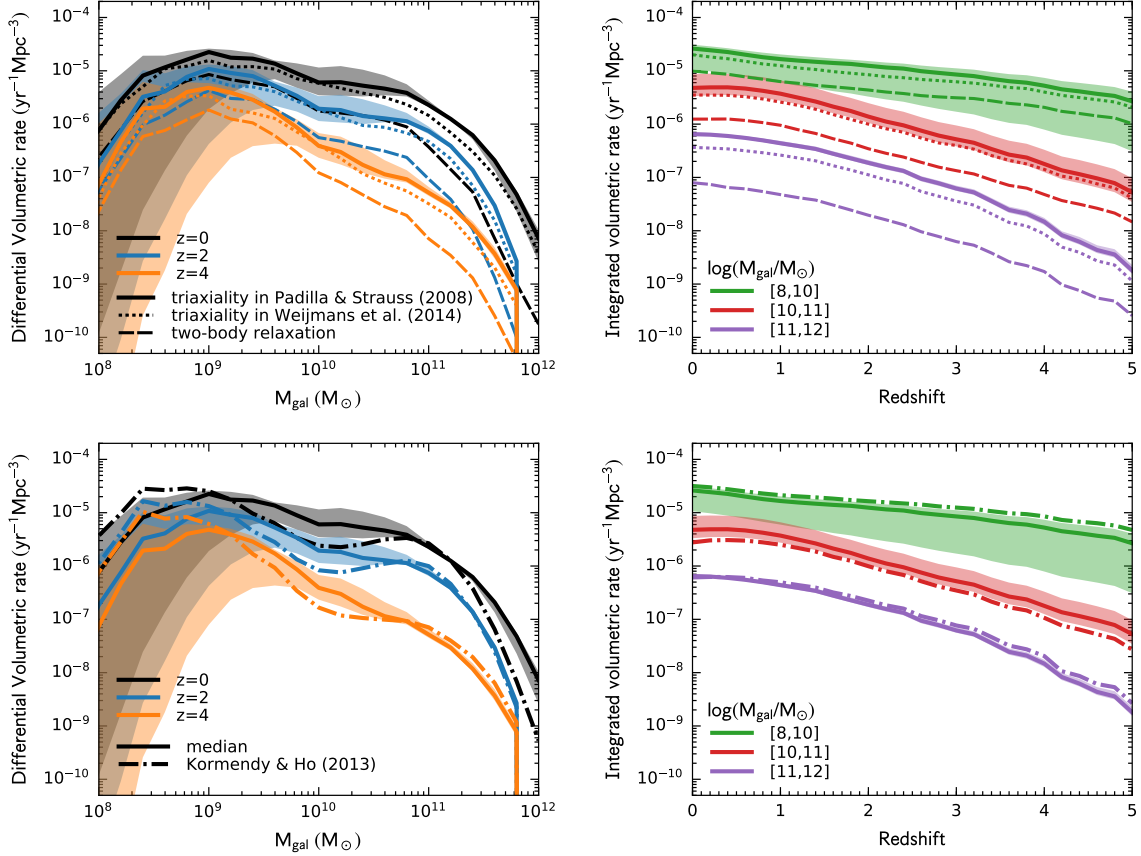


**Figure 9.** Similar to Figure 7 or 8, but excluding galaxies with MBH mass  $M_{\text{BH}} > 10^9 M_{\odot}$ . The volumetric stellar disruption rates in bright galaxies ( $\sim 6 \times 10^{-7} \text{yr}^{-1} \text{Mpc}^{-3}$  at  $z = 0$  for  $M_{\text{gal}} \gtrsim 10^{11} M_{\odot}$ ) are about 2% of the stellar tidal disruption rates in all the galaxies at  $z = 0$ .

tion rates are higher in the galaxies with steeper slopes in their surface brightness profiles for  $M_{\text{BH}} \lesssim 10^7 M_{\odot}$ , and become insensitive to the inner slope of the surface brightness profiles for higher MBH masses.

Regarding the differential volumetric consumption rate  $d\mathbb{F}_{\text{vol}}^{\text{consp}}/d\log M_{\text{BH}}$ , the increase caused by adding the effects of triaxial galaxy shapes is by a factor of  $\sim 3$  for MBHs with mass  $M_{\text{BH}} \lesssim 10^7 M_{\odot}$ . For MBHs with larger masses, the increase is larger. For example,  $d\mathbb{F}_{\text{vol}}^{\text{consp}}/d\log M_{\text{BH}}$  increases by a factor of  $\sim 5$ – $8$  at  $M_{\text{BH}} \simeq 10^8 M_{\odot}$  and by two orders of magnitude at  $M_{\text{BH}} \simeq 10^9 M_{\odot}$ , compared to the rates obtained by considering only the loss-cone refilling due to two-body relaxation in spherical gravitational potentials. The TDE flaring rates are mainly dominated by the systems with low-mass MBHs, and we have a median value of the integrated volumetric consumption rates ( $\int d\mathbb{F}_{\text{vol}}^{\text{consp}}$ )  $\sim 3 \times 10^{-5} \text{yr}^{-1} \text{Mpc}^{-3}$  for all the MBHs with  $M_{\text{BH}} \sim 10^5$ – $10^8 M_{\odot}$  at redshift  $z = 0$ , and  $\sim 1.4 \times 10^{-6} \text{yr}^{-1} \text{Mpc}^{-3}$  for MBHs within  $10^7$ – $10^8 M_{\odot}$ . The stellar swallowing rates are  $\sim 8.0 \times 10^{-7} \text{yr}^{-1} \text{Mpc}^{-3}$  for MBHs with higher

masses. Note that those estimates are based on assuming the MBHs are Schwarzschild BHs. If the MBHs are extremely spinning Kerr BHs (e.g., with the dimensionless spin parameter being 0.998), the upper mass limit of the MBH that can tidally disrupt a star with solar mass and solar radius can increase from  $\sim 10^8 M_{\odot}$  to  $\sim 10^9 M_{\odot}$  (e.g., Mummery & Balbus 2020), so that the TDE flare rates can be  $\sim 10^{-6} \text{yr}^{-1} \text{Mpc}^{-3}$  for MBHs with  $M_{\text{BH}} \sim 10^8$ – $10^9 M_{\odot}$ .

The volumetric stellar consumption rates decrease with increasing redshifts, and the decrease is relatively mild for  $M_{\text{BH}} \sim 10^5$ – $10^7 M_{\odot}$  and stronger for higher  $M_{\text{BH}}$ . Most of the stellar TDEs at  $z = 0$  occur at galaxies with mass  $M_{\text{gal}} \lesssim 10^{11} M_{\odot}$ . About 1% of the TDEs can occur at high-mass galaxies with  $M_{\text{gal}} \gtrsim 10^{11} M_{\odot}$  if all the MBHs are Schwarzschild BHs, and up to  $\sim 2\%$  of TDEs can occur at high-mass galaxies with  $M_{\text{gal}} \gtrsim 10^{11} M_{\odot}$  if all the MBHs are extremely spinning Kerr BHs.

A statistically significant result of TDEs with an MBH mass spectrum and with different galaxy properties (e.g., the inner slopes of surface brightness profiles) obtained from observations will be helpful for a comparison with the expectation from the work, e.g., to be achieved by future time-domain sky surveys (Stone et al. 2020) by expanding the TDE sample by orders of magnitude and with a sufficiently wide variety in galaxy properties. Such a comparison would provide significant constraints on the occupation number of MBHs in low-mass galaxies, the relationship between MBH mass and

host galaxy properties, and general relativistic effects on TDEs, etc.

We thank the referee for perceptive comments. This work was supported in part by the National Natural Science Foundation of China under Nos. 11673001, 11273004, 10973001, 11690024, 11873056, and 11721303; the National Key R&D Program of China (grant Nos. 2016YFA0400703, 2016YFA0400704); the Strategic Priority Program of the Chinese Academy of Sciences (grant No. XDB 23040100); and National Supercomputer Center in Guangzhou, China.

## REFERENCES

- Alexander, T. 2017, *ARA&A*, 55, 17
- Auchettl, K., Ramirez-Ruiz, E., & Guillochon, J. 2018, *ApJ*, 852, 37
- Bahcall, J. N., & Wolf, R. A. 1976, *ApJ*, 209, 214
- Behroozi, P., Wechsler, R. H., Hearin, A. P., et al. 2019, *MNRAS*, 488, 3143
- Binney, J., & Tremaine, S. 2008, Galactic Dynamics: Second Edition, by James Binney and Scott Tremaine. ISBN 978-0-691-13026-2 (HB). Published by Princeton University Press, Princeton, NJ USA, 2008.
- Bortolas, E., Gualandris, A., Dotti, M., Spera, M., & Mapelli, M. 2016, *MNRAS*, 461, 1023
- Brockamp, M., Baumgardt, H., & Kroupa, P. 2011, *MNRAS*, 418, 1308
- Cappellari, M., Emsellem, E., Krajnović, D., et al. 2011, *MNRAS*, 413, 813
- Chandrasekhar, S. 1992, The mathematical theory of black holes, New York: Oxford University Press
- Chen, X., Sesana, A., Madau, P., & Liu, F. K. 2011, *ApJ*, 729, 13
- Chen, Y., Yu, Q., & Lu, Y. 2020, *ApJ*, 897, 86, (CYL20)
- Cohn, H., & Kulsrud, R. M. 1978, *ApJ*, 226, 1087
- Cui, X., & Yu, Q. 2014, *MNRAS*, 437, 777
- Donley, J. L., Brandt, W. N., Eracleous, M., & Boller, T. 2002, *AJ*, 124, 1308
- Esquej, P., Saxton, R. D., Komossa, S., et al. 2008, *A&A*, 489, 543
- Feldmeier-Krause, A., Zhu, L., Neumayer, N., et al. 2017, *MNRAS*, 466, 4040
- Fialkov, A., & Loeb, A. 2017, *MNRAS*, 471, 4286
- Freitag, M., & Benz, W. 2002, *A&A*, 394, 345
- Freitag, M. 2003, *ApJL*, 583, L21
- French, K. D., Arcavi, I., & Zabludoff, A. 2016, *ApJL*, 818, L21
- Graur, O., French, K. D., Zahid, H. J., et al. 2018, *ApJ*, 853, 39
- Hills, J. G. 1975, *Nature*, 254, 295
- Hopman, C., & Alexander, T. 2005, *ApJ*, 629, 362
- Hopman, C., & Alexander, T. 2006, *ApJ*, 645, 1152
- Ivanov, P. B., Polnarev, A. G., & Saha, P. 2005, *MNRAS*, 358, 1361
- Kesden, M. 2012, *PhRvD*, 85, 024037
- Khabibullin, I., & Sazonov, S. 2014, *MNRAS*, 444, 1041
- Kochanek, C. S. 2016, *MNRAS*, 461, 371
- Komossa, S. 2015, *Journal of High Energy Astrophysics*, 7, 148
- Kormendy, J., & Ho, L. C. 2013, *ARA&A*, 51, 511
- Krajnović, D., Karick, A. M., Davies, R. L., et al. 2013, *MNRAS*, 433, 2812
- Lauer, T. R., Gebhardt, K., Faber, S. M., et al. 2007, *ApJ*, 664, 226
- Law-Smith, J., Ramirez-Ruiz, E., Ellison, S. L., et al. 2017, *ApJ*, 850, 22
- Lightman, A. P., & Shapiro, S. L. 1977, *ApJ*, 211, 244
- Magorrian, J., & Tremaine, S. 1999, *MNRAS*, 309, 447 (MT99)
- Maksym, W. P., Ulmer, M. P., & Eracleous, M. 2010, *ApJ*, 722, 1035
- McConnell, N. J., & Ma, C.-P. 2013, *ApJ*, 764, 184
- Merritt, D. & Quinlan, G. D. 1998, *ApJ*, 498, 625.
- Merritt, D., & Ferrarese, L. 2001, *The Central Kiloparsec of Starbursts and AGN: The La Palma Connection*, 249, 335
- Mummery, A., & Balbus, S. 2020, 2020, *MNRAS*, 497, L13
- Padilla, N. D., & Strauss, M. A. 2008, *MNRAS*, 388, 1321
- Perets, H. B., Hopman, C., & Alexander, T. 2007, *ApJ*, 656, 709
- Pfister, H., Volonteri, M., Dai, J. L., et al. 2020, *MNRAS*, 497, 2276
- Rauch, K. P., & Tremaine, S. 1996, *NewA*, 1, 149
- Rees, M. J. 1988, *Nature*, 333, 523
- Stone, N., & Loeb, A. 2011, *MNRAS*, 412, 75
- Stone, N. C., & Metzger, B. D. 2016, *MNRAS*, 455, 859

- Stone, N. C., Kesden, M., Cheng, R. M., et al. 2018, [arXiv e-prints](#), [arXiv:1801.10180](#)
- Stone, N. C., Vasiliev, E., Kesden, M., et al. 2020, [SSRv](#), [216](#), 35
- Tadhunter, C., Spence, R., Rose, M., et al. 2017, [Nature Astronomy](#), [1](#), 0061
- Touma, J., & Tremaine, S. 1997, [MNRAS](#), [292](#), 905
- van Velzen, S., & Farrar, G. R. 2014, [ApJ](#), [792](#), 53
- van Velzen, S. 2018, [ApJ](#), [852](#), 72
- Vasiliev, E., & Merritt, D. 2013, [ApJ](#), [774](#), 87
- Vasiliev, E. 2014, [Classical and Quantum Gravity](#), [31](#), 244002
- Wang, J., & Merritt, D. 2004, [ApJ](#), [600](#), 149
- Wang, T.-G., Zhou, H.-Y., Komossa, S., et al. 2012, [ApJ](#), [749](#), 115
- Weijmans, A.-M., de Zeeuw, P. T., Emsellem, E., et al. 2014, [MNRAS](#), [444](#), 3340
- Young, P. 1980, [ApJ](#), [242](#), 1232
- Yu, Q. 2002, [MNRAS](#), [331](#), 935
- Yu, Q. 2003, [MNRAS](#), [339](#), 189